

HIGH-RESOLUTION STUDIES OF THE MULTIPLE-CORE SYSTEMS TOWARD CLUSTER-FORMING REGIONS INCLUDING MASSIVE STARS

Hiro SAITO¹, Masao SAITO¹, Yoshinori YONEKURA², and Fumitaka NAKAMURA³
 saito@nro.nao.ac.jp

ABSTRACT

We present the results of C¹⁸O observations by the Nobeyama Millimeter Array toward dense clumps with radii of ~ 0.3 pc in six cluster-forming regions including massive (proto)stars. We identified 171 cores, whose radius, line width, and molecular mass range from 0.01 to 0.09 pc, 0.43 to 3.33 km s⁻¹, and 0.5 to 54.1 M_{\odot} , respectively. Many cores with various line widths exist in one clump, and the index of the line width–radius relationship of the cores and the parental clump differs from core to core in the clump. This indicates that the degree of dissipation of the turbulent motion varies for each core in one clump. Although the mass of the cores increases with the line width, most cores are gravitationally bound by the external pressure. In addition, the line width and the external pressure of the cores tend to decrease with the distance from the center of the clump, and these dependencies may be caused by the inner H₂ density structure of the clump that affects the physical properties of the cores. Moreover, the number density of the cores and the number density of young (proto)stars have a similar relationship to the average H₂ density of the clumps. Thus, our findings suggest that the cluster is formed in the clump through the formation of such multiple cores, whose physical properties would have been strongly related to the H₂ density structure and the turbulent motion of the clump.

Subject headings: Galaxy:open clusters and associations:general—star:formation—star:early type—ISM:clouds—ISM:structure—ISM:molecules

1. Introduction

Most stars in the galactic disk are formed in dense molecular gas within giant molecular clouds (GMCs) as members of clusters (Lada & Lada 2003). Thus, clusters must play a critical role in the origins of some of the most fundamental properties of the galactic stellar population. In addition, such clusters consist of stars of various masses, and the most massive stars exist at the centers of clusters (e.g., Raboud & Mermilliod

1998). These features suggest that the physical environment in the cluster-forming region would vary from area to area because the mass of formed stars should be closely related to the physical environment. However, clusters do not always include massive stars. Some clusters contain only intermediate-mass and/or low-mass stars in low-mass star-forming regions (e.g., Tachihara et al. 2002). Based on these features, it appears that although the conditions of massive star formation easily satisfy the physical conditions for cluster formation, the conditions of cluster formation do not necessarily provide the physical conditions for massive star formation.

The clusters appear to be continuously forming in the galactic disk and the direct study of their physical conditions and the processes leading to their formation is basically possible. How-

¹National Astronomical Observatory of Japan, Osawa 2-21-1, Mitaka, Tokyo 181-8588, Japan

²Department of Physical Science, Osaka Prefecture University, Gakuen 1-1, Sakai, Osaka 599-8531, Japan

³Faculty of Education and Human Sciences, Niigata University, 8050 Ikarashi2-no-cho, Niigata City 950-2181, Japan

ever, discovering clusters at an early evolutionary stage via optical observations is difficult because such clusters are completely embedded in dense gas and dust. Therefore, observation by infrared instruments is necessary to study cluster formation. Recently, many young embedded clusters within molecular clouds have been discovered by infrared observations (e.g., Bica et al. 2003). On the basis of these observations, to investigate the physical conditions in the dense gas that forms rich clusters, dense molecular gas surveys were carried out on such young clusters that include massive stars, revealing that clusters are formed in gas systems with a size scale of a cluster (~ 0.3 pc) in GMCs (e.g., Lada 1992; Lada & Lada 2003; Saito et al. 2007) and these systems are usually called “clumps.” However, a few very compact gas systems having a size scale of ~ 0.03 pc similar to typical (cold) cores in low-mass star-forming regions (e.g., Onishi et al. 2002; Umemoto et al. 2002) have been discovered with very high-angular-resolution observations using an interferometer on young clusters that include massive (proto)stars (e.g., Churchwell et al. 1992; Olmi et al. 1993). These systems have high temperatures (> 100 K), a high H_2 density (10^6 – 10^7 cm $^{-3}$), and a high luminosity ($> 10^4 L_\odot$). These results indicate that these systems called “hot cores,” would include massive protostar(s) or massive young star(s).

Generally, not a large number of stars form in a core even in cluster-forming regions (e.g., van der Tak et al. 2005). Hence, many cores must form in one clump to create a cluster with a large number of stars. If this multiple-core system is formed by the fragmentation of the inner structure of the clump, a close relationship should exist between the physical parameters of the clump and the characteristics of the formed cluster. Saito et al. (2007) carried out molecular line observations using the Nobeyama 45-m telescope directed toward the clumps in several cluster-forming regions and suggested that a good relationship indeed exists between the average H_2 density of the clumps and the stellar number density of formed clusters in these clumps. In addition, they found a good correlation between the line width of the clumps and the maximum mass of formed stars. Saito et al. (2006) investigated the cores in three cluster-forming regions and found two types of cores in

a single clump. The first type was a core with a large mass and a large turbulent motion, and the second type was a core with a small mass and a small turbulent motion. They found that massive (proto)stars are associated with the cores with a large mass and large turbulent motion. This suggests a theoretical dependence between the mass of the star formed in a core and the turbulent motion in the core (e.g., McKee & Tan 2003). According to the suggestion by McKee & Tan (2003), the results of Saito et al. (2006) indicate that massive and low-mass stars can be formed from one clump. Such observations suggest that to understand the mechanism of cluster formation, it is important to elucidate the relationships between the physical properties of cores and physical condition of the clump that includes the cores, and between the mass of the star formed in a core and the physical condition of the core. If the cores in a clump are formed by gravitational instability as the theory suggests, a strong connection must exist between the spatial distribution of the cores in the clump and the inner structure of the clump. However, no detailed relationships between the cores and the clumps have been demonstrated. In addition, although young clusters have a tendency to concentrate massive stars in the center, whether massive cores with large turbulent motion are formed in the center of the clump remains unclear.

Therefore, we must observe several clumps to obtain detailed physical parameters of both clumps and cores and reveal the relationships between the cores and the clumps themselves. To detect the cores in the clump, we must uncover the internal motion and the distribution of the H_2 column density in the clump. Thus, we need to carry out molecular line observations suitable for revealing velocity structures of the dense gas in the clump. Such observations are important to find a protocluster that consists of multiple cores — a “core cluster.”

We carried out $C^{18}O$ observations toward nine IRAS point sources with young clusters containing massive stars. The $C^{18}O$ line is a good candidate for tracing a large dynamic range in mass and column density in the dense gas because this line has a thin optical depth and a low critical density. In general, the $C^{18}O$ line cannot be used to probe high-density regions ($> 10^4$ cm $^{-3}$) in starless cores because CO molecules are depleted onto

dust grains in such a cold region with a temperature lower than the CO sublimation temperature of ~ 20 K (e.g., Caselli et al. 1999; Bacmann et al. 2002). However, previous CO observations have revealed that CO lines trace high-density regions ($> 10^4 \text{ cm}^{-3}$) well with high temperatures of $\gtrsim 20$ K (e.g., Momose et al. 1998; Schöier et al. 2004). Therefore, if the temperatures of high-density regions ($> 10^4 \text{ cm}^{-3}$) are higher than ~ 20 K, C^{18}O lines can be used to probe these regions. Typically, the regions where massive stars are formed in GMCs maintain high temperatures of $\gtrsim 20$ K, and thus C^{18}O molecules would not be depleted in such regions. In fact, the structures identified by the interferometric observations toward massive star-forming regions have a high average density of $> 10^5 \text{ cm}^{-3}$ (e.g., Hunter et al. 2004; Saito et al. 2006). Therefore, C^{18}O observations can be used to reveal the distribution, mass, and kinetic motion of the dense gas in cluster-forming regions if this line is optically thin enough.

The identification of the star-forming and starless cores requires observation with high-angular resolution of several arc-seconds because massive star-forming regions are generally located at a distance of several kpc. However, interferometric observation of C^{18}O cores in massive star-forming regions has rarely been performed. To find dense cores in the clumps with cluster formation, we carried out C^{18}O molecular line observations with high-angular resolution toward nine cluster-forming regions using the Nobeyama Millimeter Array (NMA). The physical conditions of the clumps in these regions were already derived by Saito et al. (2007). Results of the interferometric observations toward three of these nine regions were already reported in Saito et al. (2006). Here we present the results of the observations toward the other six regions. We present our millimeter interferometric observations in § 2. In § 3, the observational results are presented for millimeter continuum and C^{18}O molecular line. We discuss the implications of our results for the physical condition of the dense cores in § 4. In § 5, we summarize the main results of our study.

2. Observations

2.1. Samples

To compare the physical conditions in the dense gas around young clusters containing young massive stars with the characteristics of the clusters, we need to select targets at similar evolutionary stages and distances and with similar bolometric luminosities, because the observed physical parameters depend on both the characteristics of formed stars (e.g., Saito et al. 2001) and the spatial resolutions. In addition, the evolution of an embedded stellar cluster is sensitively coupled to the evolution of its surrounding gas (e.g., Lada & Lada 2003). Carpenter et al. (1990), Zinchenko et al. (1994, 1997, 1998), and Sridharan et al. (2002) carried out observations with low-angular resolution ($\sim 60''$) toward luminous IRAS point sources associated with $\text{H}_2\text{O}/\text{CH}_3\text{OH}$ masers and/or compact H II regions in the northern sky and identified 93 massive clumps with a size of > 1.0 pc. $\text{H}_2\text{O}/\text{CH}_3\text{OH}$ masers and/or compact H II regions serve as the indicators of very young massive stellar objects in massive star-forming regions. We selected 14 IRAS point sources from these clumps on condition that the luminosity of the IRAS source is several times $10^4 L_\odot$, the distance is $\sim 2 - 4$ kpc, and the source is associated with both the indicators of very young massive stellar objects and NIR clusters.

We observed nine of these where the physical parameters of the dense clumps were already derived by single-dish observations with high-angular resolution of $\sim 15''$ (Saito et al. 2007). In this paper, we report the observational results obtained toward six objects except for three objects that were already reported by Saito et al. (2006). These IRAS sources are associated with the indicators of very young massive stellar objects: (1) (U)C H II region(s) for IRAS 05375+3540 (e.g., Felli et al. 2006), IRAS 06117+1350 (Turner & Terzian 1985), IRAS 19442+2427 (e.g., Barsony 1989), and IRAS 19446+2505 (e.g., Gómez et al. 1995). (2) very weak centimeter continuum sources for IRAS 06056+2131, and IRAS 06061+2151 (Kurtz et al. 1994). This indicates that these massive (proto)stars are at a similar evolutionary stage within several times 10^5 yr. Table 1 lists the position, distance, and luminosity of each source.

2.2. Nobeyama Millimeter Array(NMA) Observations

The observations were carried out from November 2002 through May 2005 with the six-element Nobeyama Millimeter Array (NMA) in the C^{18}O ($J=1-0$; 109.782 GHz) line, and 98 GHz and 110 GHz continuum. The 8-h tracks were obtained in the most compact (designated as D) and intermediate (designated as C) configurations. The projected antenna baseline length ranged from 13 m to 163 m, yielding the typical resolution of $\sim 4''$ when natural weighting is applied to all visibility data. The resolution of each observation is given in Table 2. At 110 GHz, the primary beam of the 10-m telescope is about $62''$.

We used the SIS receivers, whose system noise temperatures in single sideband were ~ 400 K (including the atmosphere toward the zenith). Digital correlators UWBC and FX were configured for 1024 MHz and 32 MHz bandwidths with 128 and 1024 channels per baseline, respectively, yielding an equivalent resolution of 44 km s^{-1} and 0.1 km s^{-1} at 110 GHz, respectively. The UWBC can provide both the upper sideband (110 GHz) and the lower sideband data (98 GHz).

The gain calibrations were carried out for each upper and lower sideband every 10-15 min by observing quasars 0528+134, 0552+398, and 2023+336. The bandpass calibration was performed with 3C454.3 and 3C84. Uranus was observed at 3 mm to estimate the absolute flux scale. The uncertainties in the flux scale are about 15%.

The visibility data were calibrated using the NRO software package UVPROC2, and final maps were made using the CLEAN algorithm of the Astronomical Image Processing System (AIPS) by the National Radio Astronomy Observatory (NRAO¹). The 3-mm continuum maps are constructed from line-free channels of a 44 km s^{-1} wide window. The uncertainties of the position in the maps are about $< 1''$. The noise levels of the natural-weighted maps are summarized in Table 2.

¹The NRAO is operated by the National Science Foundation by Associates Universities, Inc., under a cooperative agreement.

2.3. Definition of C^{18}O cores

We defined a compact structure, a core, from the distribution of C^{18}O intensity to estimate physical properties of the dense condensations. We used the following procedures, similar to those adopted by Saito et al. (2007):

(1) To identify the velocity components in the observed fields, we checked the C^{18}O molecular spectrum. If the C^{18}O spectrum has more than two line features and the separations among their radial velocities are larger than 0.5 km s^{-1} , each line feature was attributed to different velocity components.

(2) We made a C^{18}O integrated intensity map for each velocity component.

(3) We searched for the i -th intensity peak (peak- i) outside previously defined cores (i.e., core[1], core[2], ..., core[$i-1$]) in the C^{18}O integrated intensity map.

(4) We drew a contour at the half-level of the intensity value at peak- i and defined the region enclosed by the half-intensity contour as a core[i].

(5) In cases when sub-peaks exist within the core[i], if the intensity at a sub-peak is larger than 6σ above the hollow between it and peak- i , we excluded the region around the sub-peak by splitting the core[i] along the hollow.

(6) In cases when previously defined cores (i.e., core[1], ..., core[$i-1$]) exist within the boundary of the core[i], if the intensity at peak- i is larger than 6σ above the hollow between peak- i and the peaks of the previously defined cores, we excluded the region around the peaks of the previously defined cores by splitting the core[i] along the hollow. Otherwise, the core[i] was canceled.

(7) We searched for the next ($[i+1]$ -th) intensity peak outside the cores.

(8) We repeated the procedures after procedure (4) until the value of the intensity of the local peak went below the 6σ noise level.

We identified 171 C^{18}O molecular cores using these procedures. The observed properties of the C^{18}O cores, such as the absolute peak temperature, T_{R}^* , the radial velocity, V_{LSR} , the FWHM line width, ΔV , at the peak position, and the composite line width, ΔV_{com} , of the core are summarized in Table 3. Here, the composite line width is the FWHM line width of the composite spectrum

made by averaging all spectra within the core. The typical uncertainties of the temperature, radial velocity, and line width in the Gaussian fits are 0.1 K, 0.1 km s⁻¹, and 0.1 km s⁻¹, respectively.

2.4. Definition of the Millimeter Continuum Sources

We next defined the millimeter continuum sources (MCSs) from the continuum images to estimate the physical properties of the very dense regions and to identify the positions of the massive (proto)stars. Therefore, we identified MCSs except the known HII regions from the 98 GHz and 110 GHz continuum maps using procedures (3)–(8) adopted by the C¹⁸O core definition. We also stipulated that the MCSs were detected at both the 98 GHz and the 110 GHz continuum bands. As a result, we identified 13 MCSs and detected six known (U)C HII regions. The observed parameters of these sources are summarized in Table 4.

3. Results

3.1. Derivation of Physical Properties of the Cores

The goal of this study was to clarify physical processes of both cluster formation and massive star formation by investigating the indispensable physical characteristics of the dense gas that forms young clusters.

In this paper, we defined a clump as a fundamental structure in which clusters are formed and defined a core as a fundamental structure in which individual stars in the cluster are formed. Previous studies (e.g., Umemoto et al. 2002; Saito et al. 2006, 2007) indicated that the clumps have a size scale of ~ 0.3 pc and the cores have a size scale of ~ 0.03 pc. The physical quantities of the dense gas in the cluster-forming regions, including massive star formations, are derived from the C¹⁸O-line emission.

3.1.1. C¹⁸O line analysis

Generally, the C¹⁸O molecule is chemically stable and the optical depth of C¹⁸O ($J = 1-0$) is very thin. Thus, this line is very useful for estimating the H₂ column density. Here, we calculate the C¹⁸O optical depth and the H₂ column den-

sity under the local thermodynamic equilibrium (LTE) condition with the excitation temperature, T_{ex} , estimated from the ¹²CO peak temperature of $T_{\text{R}}^*(^{12}\text{CO}) = 31 - 56$ K at the position of each maser source (Barsony 1989; Wouterloot & Brand 1989; Zinchenko et al. 1998; White & Fridlund 1992). We assume that the excitation temperature of each core is the same as that at the position of the maser source in each region. In these cases, the excitation temperatures, T_{ex} , were estimated to be 35 – 60 K. With these excitation temperatures, the C¹⁸O optical depth, $\tau(\text{C}^{18}\text{O})$, and C¹⁸O column density, $N(\text{C}^{18}\text{O})$, were estimated using

$$\tau(\text{C}^{18}\text{O}) = -\ln \left\{ 1 - \frac{T_{\text{R}}^*(\text{C}^{18}\text{O})}{5.27} \left[\frac{1}{\exp(5.27/T_{\text{ex}}) - 1} - 0.166 \right]^{-1} \right\},$$

and

$$N(\text{C}^{18}\text{O}) = 2.42 \times 10^{14} \times \left\{ \frac{\tau(\text{C}^{18}\text{O}) \Delta V (\text{km s}^{-1}) T_{\text{ex}}}{[1 - \exp(-5.27/T_{\text{ex}})]} \right\} (\text{cm}^{-2}) \quad (2)$$

(e.g., Rohlfs & Wilson 2004), where $T_{\text{R}}^*(\text{C}^{18}\text{O})$ is the C¹⁸O radiation temperature in kelvins. We calculated the H₂ column density, $N(\text{H}_2)$, assuming that the C¹⁸O abundance ratio is 1.7×10^{-7} (Frerking et al. 1982). The C¹⁸O optical depth and H₂ column density at the intensity peak of the cores range from 0.02 to 0.19 and from 0.8×10^{22} to 2.4×10^{23} cm⁻², respectively. From these results, we found that the optical depth of the C¹⁸O line is very thin.

3.1.2. The Physical Parameters of the Cores

First, we estimated the line width and the radius of the cores. We regard the line width of the composite line profile as the line width of the core. The line width of the cores ranges from 0.43 to 3.33 km s⁻¹ with a mean line width of 1.08 km s⁻¹.

We estimated the radius of the cores assuming that the cores are spherical. We defined the radius of the core, R_{core} , as the deconvolved radius and calculated it as

$$R_{\text{core}} = \sqrt{\frac{S - \text{beam area}}{\pi}}, \quad (3)$$

where S and beam area are the area inside the core and the area of the synthesized beam, respectively. The radius ranges from 0.010 to 0.090 pc, with a

mean radius of 0.035 pc. We selected the cores with the ratio of the deconvolved radius to the observed radius of > 0.5 to select the cores resolved by the present observations. Note that we call the radius calculated from $(S/\pi)^{1/2}$ the “observed radius.” Hereafter, we use only the cores with high reliability for discussions involving the radius.

Next, we estimated the LTE mass, M_{core} , and the average H_2 density, $n(\text{H}_2)_{\text{core}}$, of the cores. The LTE mass of the cores was derived by integrating the H_2 column density over the core. We assumed a mean molecular weight per one H_2 molecule of 2.8 by taking into account a relative helium abundance of 25% by mass. The average H_2 density of the core is derived by assuming both a spherical shape and a uniform density and estimated by dividing the mass by a core volume, $(4/3)\pi R_{\text{core}}^3$. The LTE mass and the average H_2 density of the cores range from 0.5 to $54.1 M_{\odot}$ and 0.6×10^5 to $2.1 \times 10^6 \text{ cm}^{-3}$, respectively.

Finally, we estimated the virial mass, M_{vir} , of the cores. The virial mass is one of the key quantities by which we can evaluate the equilibrium state of the cores. The virial mass of the core is derived using the following equation, assuming isothermal, spherical, and uniform density distribution with no external pressure or magnetic forces:

$$M_{\text{vir}} = \frac{5 R_{\text{core}}(\Delta V_{\text{com}})^2}{8 G \ln 2}, \quad (4)$$

where G is the gravitational constant. The virial mass of the cores ranges from 0.7 to $143.4 M_{\odot}$. These physical properties are summarized in Table 5.

3.2. Star-forming Cores and Starless Cores

Here, we distinguish starless cores and star-forming cores to investigate the star-formation activity in C^{18}O cores in cluster-forming regions. We compared the cores with near infrared sources (2MASS² sources), MCSs, and centimeter continuum sources (CCSs) as indicators of young stellar objects to reveal star formation in the cores.

²The Two Micron All Sky Survey (2MASS) is a joint project of the University of Massachusetts and the Infrared Processing and Analysis Center/California Institute of Technology, funded by the National Aeronautics and Space Administration and the National Science Foundation (<http://pegasus.phast.umass.edu>).

In particular, we selected the 2MASS sources detected at more than or equal to two bands with $A_V > 10$ mag among the sources associated with the clumps (Saito et al. 20007) because the sources embedded in the dense gas must have a large extinction such that the typical peak H_2 column density of the C^{18}O cores is more than $1 \times 10^{22} \text{ cm}^{-2}$. Note that the 2MASS sources identified by Saito et al. (2007) include young stellar objects (YSOs), which are the class I – III type sources, and background sources. Here, we define an association as when an intensity peak of one object is located inside the boundary of the other object. Note that the cores associated with only MCSs are possibly very massive and dense starless cores.

First, we compared 13 MCSs with CCSs and 2MASS sources. Three of these are associated with both 2MASS sources and CCSs, and four of 13 MCSs are associated only with 2MASS sources. Only one of 13 MCSs, MCS B for IRAS 06056+2131, is associated only with CCSs and is seen as a dark lane in the K_s -band image in Figures 2(b) and (c). The flux density of the CCSs associated with MCSs corresponds to that of the H II region formed by a B2–3 star or of the ionized stellar wind formed by a B0–1 star (e.g., Panagia 1973; Felli & Panagia 1981). Therefore, the CCSs associated with MCSs would be caused by the activity of massive YSOs.

We also derived spectral indices of MCSs from 98 GHz and 110 GHz data in Table 6. The spectral index of 8 MCSs with 2MASS sources and/or CCSs ranges from 2.2 to 4.6. This indicates that the millimeter continuum emission from these MCSs is subject to thermal dust radiation. Thus, the four MCSs with CCSs indicate the existence of young massive (proto)stars. Three other MCSs only associated with 2MASS sources except for MCS A for IRAS 19442+2427 have a strong intensity peak in millimeter continuum emission, and 2MASS sources associated with these MCSs have the brightness corresponding to an early B type or earlier star. Therefore these three MCSs would include early B type or earlier (proto)stars. Indeed, two of these MCSs, MCS A for IRAS 05375+3540 and MCS A for IRAS 06117+1350, have a high luminosity of $\sim 1 \times 10^3 L_{\odot}$ (corresponding to a B3–4 star) and $\sim 7 \times 10^4 L_{\odot}$ (corresponding to a O9.5 star), respectively (Eiroa et al. 1994; Felli et

al. 2004). Although the 2MASS source associated with MCS A for IRAS 19442+2427 has a brightness corresponding to an early B star, this MCS has no strong intensity peak in millimeter continuum emission and the total integrated continuum emission from the MCS is very weak. In addition, although this MCS has a large H_2 column density ($\sim 10^{23} \text{ cm}^{-2}$), the associated bright 2MASS source has no large extinction ($A_V < 30$). Thus, this 2MASS source would be located in front of the MCS.

However, four of five MCSs with neither 2MASS sources nor CCSs, MCSs A, B, and C for IRAS 19446+2505 and MCS C for IRAS 19442+2427, have a flux density of 110 GHz similar to or smaller than that of 98 GHz, and the spectral indices of these four MCSs are to be in the range between -2.9 and $+0.6$ in Table 6. In particular, three MCSs for IRAS 19446+2505 are located at the edge of the optical H II region, S88B. Thus, we regard these four MCSs as consisting of only free-free emission. Note that MCS B for IRAS 19446+2505 with a large negative index of -2.9 is more extended diffusely than the other MCS. Generally, it is probable that the missing flux of the 110 GHz observation is larger than that of the 98 GHz observation for a diffuse extended source because the minimum UV length of the 110 GHz observation is longer than that of the 98 GHz observation. Therefore, the MCS B would have such a negative index. Thus, we regard this MCS as a source consisting of only free-free emission. The other MCS with neither 2MASS sources nor CCSs, MCS B for IRAS 19442+2427, has a strong intensity peak and a large spectral index of ~ 3.7 , which is similar to that of the other massive-star-forming MCSs. Hence, in this paper, we regard this MCS as a source with massive protostars.

Next, we compared 171 C^{18}O cores with MCSs, 2MASS sources, and CCSs. Eight of the cores are associated with both MCSs and 2MASS sources and two of 171 cores are associated only with MCSs. In addition, 19 of 171 cores are associated only with 2MASS sources. From this result, all MCSs except for four MCSs classified as F.F. (see Table 6) are associated with C^{18}O cores. However, cores N and R for IRAS 19442+2427 are associated with same 2MASS source and same MCS, MCS A. The intensity distribution of the MCS corresponds to the part with the high H_2 column

density of these cores in Figures 5(b) and (d). The MCS would be associated with high-density part of these cores. Therefore, cores N and R for IRAS 19442+2427 with MCS A, which consist of cold dust emission, would be starless cores rather than cores with massive YSOs. From these results, we regard 27 cores associated with 2MASS sources and/or MCSs except for cores N and R for IRAS 19442+2427 as star-forming cores. In particular, we regard eight star-forming cores associated with MCSs that include massive protostars as massive-star-forming cores.

Therefore, we identified 27 star-forming cores, including eight massive-star-forming cores. These results are summarized in Table 5. Note that the NIR source associated with these cores is not necessarily a (proto)star itself, and the possibility exists that this NIR emission is a reflection nebula of one or more central heating source(s). In addition, it may be probable that some of the cores cataloged as starless are associated with mid-IR sources.

3.3. Mass of the Continuum Sources

Generally, the 98 and 110 GHz continuum emissions consist of free-free emission and/or thermal dust emission. First, we derived the flux of thermal dust component in MCSs with CCSs. The flux density of CCSs are much smaller than the total flux of MCSs at the millimeter wavelength as shown in Table 4. The spectral indices at 100 GHz of UC H II regions and ionized winds are usually ~ -0.1 and ~ 0.5 (e.g., Panagia & Felli 1975), respectively. We assumed that these CCSs consist of the free-free emission with a spectral index of 0 from an optically thin H II region or ionized winds, and we estimated the flux of thermal dust component in MCSs by subtracting the contribution of the free-free emission from the total flux of MCSs.

Next, we estimate the physical properties of the MCSs. The deconvolved radii of the MCSs, R_d , are calculated using equation (3). The estimated radius of MCSs ranges from 0.018 to 0.110 pc. In particular, the radius of the MCSs associated with C^{18}O cores ranges from 0.018 to 0.055 pc and is smaller than that of the associated cores ($R_d/R_{\text{core}} \sim 0.8$). In addition, assuming an optically thin dust thermal emission at 100 GHz, we

estimated the mass of MCSs using

$$M_d = \frac{F_\nu D^2}{\kappa_\nu B(\nu, T_d)}, \quad (5)$$

where M_d is the gas and dust mass of an MCS, F_ν is the total flux of the MCS, $B(\nu, T_d)$ is the Planck function with the assumed dust temperature, T_d , and $\kappa_\nu = \kappa_{230\text{GHz}} \left(\frac{\nu}{230\text{GHz}}\right)^\beta$ is the dust opacity per gram with $\kappa_{230\text{GHz}} = 0.005 \text{ cm}^2 \text{ g}^{-1}$ (Preibisch et al. 1993), which assumes a standard gas-to-dust mass ratio of 100. Here, we assume that the dust opacity index, β , of the dust in MCSs is 1.5 and that the dust temperature is equal to the temperature of the gas. First, we need to determine the temperatures of MCSs to estimate the mass of MCSs. The temperature of MCSs A and B for IRAS 05375+3540 were estimated by Felli et al. (2004) using CH_3CN lines, and we use this temperature as the dust temperature of the MCS. Next, because no observation has been carried out toward the other MCSs using molecular lines, which trace the gas temperatures such as CH_3CN and NH_3 , we estimate the temperature of MCSs with massive star formation to be $\sim 54 - 77 \text{ K}$ by applying the Stefan–Boltzmann law using the luminosity of (proto)stars associated with the MCSs. If we estimate the temperature of MCSs A and B for IRAS 05375+3540 using the same method, the temperature of $\sim 30 \text{ K}$ is obtained, which is similar to the temperature derived by molecular line described above. Finally, concerning MCS A for IRAS 19442+2427 without massive star formation, we use the excitation temperature estimated from the ^{12}CO peak temperature as the dust temperature. We estimate the mass of MCSs using these dust temperatures and the mass of the MCSs ranges from ~ 2.7 to $111 M_\odot$. We estimate the average H_2 density of the MCSs using the radius and the mass of the MCSs, and the average H_2 density ranges from 1.0×10^6 to $8.1 \times 10^6 \text{ cm}^{-3}$.

3.4. Individual Regions

The integrated intensity maps of C^{18}O as well as various kinds of objects related to star formation are given in Figures 1 – 6. For each region, the distribution of C^{18}O clumps, which were taken from Saito et al. (2007), IRAS sources, H_2O masers, H II regions, and the primary beam area of the present NMA observation are given in Figure (a). In addition, the physical properties of

the clumps are summarized in Table 7. The integrated intensity distribution of C^{18}O in the clumps is compared with the 98 GHz or 110 GHz continuum image in Figure (b). In Figure (c), the C^{18}O distribution is overlaid on the 2MASS K_s -band image. The distribution of C^{18}O cores, CCSs, and MCSs are given in Figure (d). The strong peak in the continuum image indicate massive (proto)stars embedded in dense gas and the K_s -band sources associated with cores indicate young stars or protostars. In addition, although each missing flux in the NMA primary beam area is roughly estimated to be $\sim 70\%$ using the single dish observation data (Saito et al. 2007), the missing flux toward the present C^{18}O cores is small to be $\sim 30\%$. This suggests that the missing flux of the present observations would be caused by the structure more extended than the size of the one measured with the present observations. As the interferometer filters out the extended emission and C^{18}O observations can detect the dense gas, the present observations would accurately detect compact cores in a clump. In the following sections, we present descriptions of the individual regions.

3.4.1. IRAS 05375+3540 (GL 5162, S235A/B)

In Figure 1, we identified 21 C^{18}O cores and two MCSs in three clumps, clumps B, C, and D identified by Saito et al. (2007). In addition, we detected free-free emission from a part of the H II region, S235 A (e.g., Felli et al. 2006), by the present continuum observation. C^{18}O core J is associated with MCS A and a bright 2MASS source. Although this 2MASS source is associated with the intensity peak of MCS A, the intensity peak of core J has an offset by $\sim 4''$ from this 2MASS source. C^{18}O core H is associated with MCS B, a bright 2MASS source, and a CCS (Felli et al. 2006).

3.4.2. IRAS 06056+2131 (GL 6336s)

In Figure 2, we identified 19 C^{18}O cores and two MCSs in clump A identified by Saito et al. (2007). C^{18}O core E is associated with MCS A and a bright 2MASS source. Although the intensity peak of MCS A is associated with this 2MASS source, the intensity peak of core E has an offset by $\sim 6''$ from this 2MASS source. C^{18}O core J is associated with MCS B and two CCSs and the

intensity peak of this core is associated with a dark lane in the K_s -band image.

3.4.3. *IRAS 06061+2151 (GL 5182)*

In Figure 3, we identified 24 $C^{18}O$ cores and two MCSs in clump B identified by Saito et al. (2007). $C^{18}O$ core O is associated with MCS B, two CCSs, and two bright 2MASS sources. The intensity peak of this core is associated with one of these CCSs and is located between these 2MASS sources. $C^{18}O$ core P is associated with MCS A, a CCS, and a bright 2MASS source. The intensity peak of core P has an offset by $\sim 2''$ from this CCS. In addition, this CCS has a larger flux density (~ 3.4 mJy) than that (~ 0.6 mJy) of the CCSs associated with core O.

3.4.4. *IRAS 06117+1350 (GL 902; S269)*

In Figure 4, we identified 28 $C^{18}O$ cores and one MCS in two clumps, clumps C and D identified by Saito et al. (2007). We also detected the free-free emission from a part of the H II region, S269 (e.g., Turner & Terzian 1985), by the present continuum observation. The intensity peak of $C^{18}O$ core M is located at both an intensity peak of MCS A and the position of a bright 2MASS source, IRS 2w. According to the luminosity of IRS 2w ($\sim 7 \times 10^4 L_\odot$), $C^{18}O$ core M may have an embedded massive (proto)star.

3.4.5. *IRAS 19442+2427 (GL 2454; S87)*

In Figure 5, we identified 38 $C^{18}O$ cores, three MCSs in three clumps, clumps A, B, and C identified by Saito et al. (2007). In addition, we detected the free-free emission from both the core and the extended structure of H II region S87 (e.g., Barsony 1989). Two velocity components, 21 km s^{-1} and 24 km s^{-1} components, exist in this region, and it has been suggested that the cluster, GL 2454, was formed by the cloud-cloud collision of these components (Saito et al. 2007). $C^{18}O$ cores, cores R, U, and AC, around the core structure of H II region S87 have a large mass ($\sim 10 M_\odot$) and a large line width ($\sim 1.5 \text{ km s}^{-1}$). $C^{18}O$ core AH is associated with MCS B, which has a strong intensity peak and a large spectral index, although this core is not associated with bright 2MASS sources. This indicates that the core could harbor an embedded massive YSO(s). In addition,

the position of the intensity peak of this core in 20.7 km s^{-1} component map has changed from that in 21.4 km s^{-1} component map in Figure 5(d), and MCS B is located between the intensity peak in each component map. This indicates that core AH has a velocity gradient and could have a disklike system embedded in it. We suggest that this embedded massive YSO(s) in MCS B (see § 3.2) would be a massive protostar.

3.4.6. *IRAS 19446+2505 (GL 2455; S88B)*

In Figure 6, we identified 41 $C^{18}O$ cores, three MCSs in two clumps, clumps B and C identified by Saito et al. (2007). In addition, we detected millimeter continuum emission, which corresponds to two compact H II regions S88B1 and S88B2 (e.g., Gómez et al. 1995). The distribution of the $C^{18}O$ emission is consistent with that of the dark region in the K_s band. $C^{18}O$ cores, cores Q and W, around the compact H II region S88B1 have a large mass ($\sim 20 M_\odot$) and a large line width ($\sim 2.0 \text{ km s}^{-1}$). Three MCSs exist at the boundary between the dense molecular gas and the optical H II region S88B. This indicates that the surface of the dense molecular gas would be ionized by the UV radiation from the massive stars in GL 2455.

4. Discussion

4.1. Physical Conditions of $C^{18}O$ Cores

Saito et al. (2007) identified 39 clumps with a size scale of ~ 0.3 pc in cluster-forming regions including massive star formation, and discussed their physical conditions by analyzing the correlations between the physical quantities of the clumps. They found that the average H_2 density of the clumps increases with the line width and the clumps are self-gravitationally bound because they have a virial mass comparable to a gas mass. Here, we extend their analysis to the inner structure of the clumps (i.e., dense cores) and attempt to clarify the physical condition of the dense cores that are the direct site of each star formation in the cluster-forming region.

First, we analyzed the relationships among the physical parameters of the cores. We used 171 $C^{18}O$ cores identified in this study and 28 $C^{18}O$ cores identified by Saito et al. (2006). The cores identified by Saito et al. (2006) were classified

into three massive-star-forming cores, seven star-forming cores, and 18 starless cores using the classification adopted in this study. These cores exist in 18 dense clumps identified by Saito et al. (2007). Next we discuss the physical conditions of the dense cores inside the clumps in cluster-forming regions including massive star formation.

4.1.1. Line Width – Radius Relationship

The line width of molecular line emissions provides us with internal kinetic properties such as thermal motion and turbulence. Several studies have suggested that a correlation exists between the line width and the radius of the core/cloud in the form of a single power-law relationship $\Delta V \sim R^\alpha$; ΔV and R are a characteristic line width and the radius of the core/cloud (e.g., Larson 1981). In addition, the index α has recently been shown to depend on the environment (e.g., Caselli & Myers 1995; Saito et al. 2006).

The left panel of Figure 7 shows the relationship between the line width and the radius of the 181 cores with high reliability (see § 3.1.2) identified by this work and Saito et al. (2006) and 18 clumps identified by Saito et al. (2007). Note the other 18 cores are those with a large error in the radius in § 3.1.2. Although the line width of the clumps is in a narrow range of 1.5 to 3.2 km s⁻¹, the line width of the cores is in a much wider range of 0.43 to 3.33 km s⁻¹. In contrast, the range of the radius of the cores is relatively small. Such features are seen even in the individual regions in the right panels of Figure 7.

We investigated the index α of the relationship between the line width and the radius of the core and the parental clumps. We estimated this relationship, $\Delta V_{\text{core}} = \Delta V_{\text{clump}} \times (R_{\text{core}}/R_{\text{clump}})^\alpha$, for all cores. The index α of this relationship ranges from 0.06 to 0.89 and the long- and the short-dashed lines in Figure 7 indicate the line width–radius relationships with the minimum and maximum index α , respectively, using a mean line width and a mean radius of the clumps in the plots. Our results show that the relationship between the line width and the radius does not follow a single power-law relation. This trend agrees with the result of Saito et al. (2006), who used a smaller number of cores and clumps. This indicates that the degree of the dissipation of the turbulent motion varies even within a single clump.

As discussed below in § 4.1.3, this may be due to the difference in the initial H₂ density or the external pressure of the core. We postulate that the difference in the dissipation of the turbulent motion depends on the region where the core is formed in the clump, considering that the clump generally has a density structure.

4.1.2. Stability of Cores in the Dense Clump

Generally, a core has to be gravitationally bound to result in star formation. Thus, a core with a large line width needs to have a large mass or high external pressure for star formation to occur. Here, we check the virial condition of the cores to investigate the stability of the system. Figure 8 shows correlations among the LTE mass, M_{LTE} , and the virial mass, M_{vir} , for 181 cores. Most of the cores have a larger virial mass than the LTE mass, and no clear difference is seen between star-forming cores and starless cores. The cores have a virial ratio (the ratio of the virial mass to the LTE mass) of ~ 2 , although several massive-star-forming cores have somewhat larger virial ratios of ~ 4 .

Generally, more extended structures with star formation (such as clumps) have a similar virial mass to a LTE mass (Fontani et al. 2002; Saito et al. 2007). The main reason for the difference in the virial ratio between the clumps and the cores is the elapsed time after the structures were formed. The virial mass of the clump just after formation would be also larger than the LTE mass and the clump would be gravitationally bound by the external pressure. The virial mass of the clump will later become similar to the gas mass because the density structure and the internal kinetic motion of the clump change and cluster formation is expected to occur in the clump. Therefore, almost all of the clump would be virialized as far as we observe the clumps with cluster formation. However, many cores would also exist just after formation in the clump. Thus, many “young cores,” which have a larger virial mass than the gas mass, could be detected by the present observation.

In addition, the virial mass of the cores, except for massive-star-forming cores, is approximately fitted by a single power-law function by

$$\log(M_{\text{vir}}) = (0.17 \pm 0.03) + (1.11 \pm 0.04) \log(M_{\text{LTE}}), \text{ C.C.} = 0.87, \quad (6)$$

where C.C. is a correlation coefficient. The coefficient of this relationship is close to unity, indicating that in the virial equation (see below), the difference in the gravitational and kinetic energy terms is almost proportional to the gravitational energy terms. To strike a good balance between this difference and the external pressure and for more massive cores to achieve the equilibrium state, the external pressure on the surface of the cores must be larger.

Most of the cores require external pressure to maintain the structures. Here, we estimate the external pressure required to bind the present cores gravitationally. The virial equation is expressed by neglecting the magnetic fields as follows:

$$F = 2U + \Omega - 4\pi R_{\text{core}}^3 P_{\text{ex}}; (U = \frac{1}{2} M \sigma^2, \Omega = -\frac{3}{5} G \frac{M^2}{R_{\text{core}}}), \quad (7)$$

where U and Ω are the kinetic and gravitational energy of the core, respectively, P_{ex} is the external pressure on the core surface, and G and σ are the gravitational constant and the velocity dispersion, $\Delta V_{\text{com}} / (2\sqrt{(2\ln 2)/3})$. The external pressure required to bind the core gravitationally, P_{R}/k , can be estimated using these equations with $F=0$. The required pressure of the cores with a virial ratio of > 1.0 ranges from 1.3×10^5 to 4.3×10^8 K cm $^{-1}$.

Next, we investigated the external pressure on the core surface. Since the external pressure is difficult to estimate, we used the average pressure in a clump (average clump pressure) $\overline{P_{\text{CL}}}/k$ instead, although these values generally differ from each other. The average clump pressure was estimated using both the line width, ΔV_{clump} , and the average H $_2$ density, $\overline{n(\text{H}_2)_{\text{clump}}}$, of the clump. We estimated the average clump pressure using the parameters of the clumps identified by Saito et al. (2007) in Table 7 and found that the average clump pressure ranges from 1.1×10^7 to 1.9×10^8 K cm $^{-1}$. Figure 9 shows the required pressure of cores plotted against the projected distance from the center of the clump to the core (core distance), R_{cen} . Here, the required pressure and the core distance are normalized to the average clump pressure and the radius of the clump, R_{CL} , respectively. We found that the required pressure for most of the cores, except for massive-star-forming cores, is smaller than the average clump pressure. Therefore, our findings suggest that most of the

cores are likely to be gravitationally bound by the external pressure.

Finally, we investigated how the required pressure of cores changes with the position in a clump. In Figure 9, the cores with a large $P_{\text{R}}/\overline{P_{\text{CL}}}$ are concentrated in the center of the clump. Therefore, the nearer the cores are to the center of the clump, the higher the external pressure on the core surface is expected to be. When the H $_2$ density structure of the clump follows $n(\text{H}_2)_{\text{clump}} \propto R_{\text{cen}}^{-\gamma}$, the pressure in the clump (clump pressure), $\overline{P_{\text{CL}}}$, is estimated as a function of R_{cen} by $\overline{P_{\text{CL}}}/\overline{P_{\text{CL}}} = (1 - \gamma/3)(R_{\text{cen}}/R_{\text{CL}})^{-\gamma}$. Here, we assumed that the turbulent velocity is constant within the clump. For comparison, the distributions of the clump pressure for $\gamma = 1.0, 1.5$, and 2.0 are indicated in Figure 9 by the dotted, solid, and dashed lines, respectively. These lines are similar to the upper limit of the $P_{\text{R}}/\overline{P_{\text{CL}}} - R_{\text{cen}}/R_{\text{CL}}$ plot, which indicates that almost all cores would be gravitationally bound by the external pressure if the H $_2$ density structure in the clump has a relation of $n(\text{H}_2)_{\text{clump}} \propto R_{\text{cen}}^{-\gamma}$. In addition, these results suggest that the external pressure of the core surface would depend on the H $_2$ density structure in the clump.

4.1.3. Mass – Line Width Relationship

Here, we investigated the relationship between the LTE mass and the line width of the core. Figure 10 shows that the LTE mass of the cores increases in proportion to the square of the line width, although the dispersion of the plot is large. This tendency agrees with the result of § 4.1.2: from equations (4) and (6), we obtain the relationship $M_{\text{LTE}} \propto (\Delta V_{\text{core}})^2$ considering that the radius of the cores is almost constant. From this tendency, dense gas with a large kinetic motion in a clump seems to be necessary to form massive cores because the LTE mass of the cores increases with the line width.

Figure 10 also indicates that no clear difference exists between star-forming and starless cores, although several massive-star-forming cores (black circles) have somewhat larger line widths than the other cores with a similar mass. For example, the average line widths of massive-star-forming cores and the starless cores (massive starless cores) with a mass $> 16 M_{\odot}$ are calculated as 2.8 km s^{-1} and 2.0 km s^{-1} , respectively. The main cause of

the difference in the line width is supposed to be the effect of star formation. If massive stars in massive-star-forming cores have formed from massive starless cores with a similar mass of $16 M_{\odot}$, the increase in momentum due to star formation is roughly estimated to be $\sim 13 M_{\odot} \text{ km s}^{-1}$. The estimated increase in momentum is much smaller than the outflow momentum supplied by massive protostar(s). For example, the total outflow momentum supplied by massive protostar(s) with a luminosity of $\sim 10^4 L_{\odot}$ is estimated to be $\sim 100 M_{\odot} \text{ km s}^{-1}$ (Zhang et al. 2005). This indicates that at most only a tenth the total outflow momentum is injected to the present core, and almost all of the outflow momentum is likely to be supplied into the intercore gas or outside the clump. In other words, massive-star-forming cores should have a large line width even prior to star formation. Therefore, we suggest that although star formation activity tends to enhance the line width of the cores, massive starless cores should form from a dense gas with a large kinetic motion.

Finally, considering that the range of the radius of the cores is small, the relationship between the mass and the line width of the cores suggests that the average H_2 density of the cores would increase with the line width of the cores. According to this result and the discussion on the external pressure in § 4.1.2, a small dissipation of the turbulent motion is sufficient for a core formed in the center of the clump with the H_2 density structure to be gravitationally bound because the initial condition of this core necessarily has a high H_2 density and a high external pressure. In this case, the index α of the line width–radius relationship from the clump to the core would become very small (~ 0.06). However, a core formed at the edge of the clump must undergo a large dissipation of turbulent motion to be gravitationally bound, and the index α would become large (~ 0.9). In other words, the physical parameters of the core would depend on the place where the core is formed in the clump. This relationship is discussed in detail in § 4.2.2.

4.2. Relationship among Young Stars, Dense Cores, and Dense Clumps

Here, we discuss the relationships between the mass of the star formed in the core and the physical parameters of the core and between the physical parameters and the positions of the cores in the

clump. Generally, the mass of a star is expected to depend on the physical properties of the parental core in a clump. Thus, the characteristics of the stellar member of the cluster would depend on the characteristics of the cores in the clump. In addition, Saito et al. (2007) found that the maximum mass of the stars associated with the clump increases with the line width of the clump and that a good correlation exists between the stellar number density of the cluster and the average H_2 density of the clump. These results indicate the importance of revealing the relationships among the clump, the cores, and young (proto)star(s) to investigate both cluster formation and massive star formation.

4.2.1. Relationship between the Mass of Formed Stars and the Physical Properties of Cores

Typical massive-star-forming cores have a higher H_2 density, larger line width, and higher temperature than the low-mass star-forming cores (e.g., Churchwell et al. 1992; Olmi et al. 1993). Although many observations with such tendencies have been reported, the relationship between the mass of the star and the physical properties of the parental core has never been quantitatively investigated. The main reason is that the discovery of the cores forming stars with various masses in the same region has been very difficult. However, typical stellar clusters have many stars with various masses, and stars formed in star-forming cores described here are expected to have a wide range of masses. Therefore, we estimated the stellar masses of the stars using the same method as Saito et al. (2007). For stars whose luminosities have been estimated or stars with centimeter-continuum sources, we estimated their spectral types using these parameters. We estimated the spectral types of other stars from the $H - K_S/K_S$ color-magnitude diagrams using the 2MASS catalog.

Figure 11 shows the relationships between the mass of (proto)stars associated with cores, M_* , and the physical parameters, LTE mass and line width, of the cores. A tendency exists for the mass of stars to increase with these parameters. These results indicate that the mass of the star would depend on the mass (or the H_2 density) and internal kinetic motion of the parental core. Generally, high average H_2 density and large inter-

nal kinetic motion would be expected to lead to a high mass accretion rate (e.g., McKee & Tan 2003). Although the plot of the relationship between the mass of the stars and the mass of the cores has a large scattering, the plot can roughly be expressed by the relationship of $M_* = M_{\text{core}}$, which is indicated by the solid line. From this relationship, the star-formation efficiency (SFE) is roughly constant at $\sim 50\%$ using the equation of $\text{SFE} = M_*/(M_* + M_{\text{core}})$. Note that the mass of the core is expected to decrease with the age of the protostar(s).

Based on the above relationships and the mass–line width relationship in § 4.1.3, the magnitude of internal kinetic energy of the core would determine the mass of the formed stars. In addition, the core must have existed in the clump at least during the lifetime of the clump for star formation to occur therein. It is therefore necessary for the core to be gravitationally bound. From these results, we suggest that the necessary and sufficient condition to form a higher mass star is that the core has a larger internal kinetic motion and is gravitationally bound. In this case, it is not necessary for the core to be self-gravitationally bound if high external pressure is brought to bear on the core surface. Because the internal kinetic motion basically decreases with time, a structure such as a molecular cloud much larger than a core or a clump must previously have had a large internal kinetic motion and must be gravitationally bound for massive star formation to occur. Thus, GMCs and clouds with an external effect, for example, H II regions and supernova remnants, would be good environments for massive star formation because such clouds would have a large external pressure and be supplied with large kinetic energy.

4.2.2. Relationship between the Cores and the Clumps

Here, we discuss the spatial distribution of the physical parameters of the cores in the clump. In § 4.1, we found that dense gas with a large kinetic motion in a clump seems to be necessary to form massive cores, and the external pressure on the surface of cores must be large for massive cores to achieve an equilibrium state. In addition, cores with large external pressure are concentrated in the center of the clump. Thus, the physical properties of the core are expected to depend on the

physical condition of the region where the core is formed in the clump.

First, we examined the relationship between the physical parameters, line width and LTE mass, of the cores and the core distance (see § 4.1.2). Figure 12(a) shows the masses of the cores plotted against the core distance. Although no clear tendency is seen in this plot, the upper limit of the core mass would gradually decrease with the core distance. If the average H_2 density of the cores is proportional to the H_2 density in the clump having a density structure of $\sim R_{\text{cen}}^{-\gamma}$, at the region where the core was formed, the core mass can be expressed by the relationship

$$M_{\text{core}} = \frac{4\pi}{3} R_{\text{core}}^3 \mu' m_{\text{H}} n(\text{H}_2)_{\text{core}} = \frac{4\pi}{3} R_{\text{core}}^3 \mu' m_{\text{H}} C n_0 \left(\frac{R_{\text{cen}}}{R_{\text{CL}}}\right)^{-\gamma} \quad (8)$$

where μ' and m_{H} are the mean molecular weight per one H_2 molecule and the hydrogen mass, respectively, and n_0 and C are the H_2 density in the clump at the distance of R_{CL} from the center of the clump and the proportional coefficient, respectively. Generally, the H_2 density structure of a clump is suggested to have a relationship with $(R_{\text{cen}}/R_{\text{CL}})^{-\gamma}$ ($\gamma \sim 1.0$ – 2.0 ; e.g., van der Tak et al. 2000). Here, if a clump has a mass of $300 M_{\odot}$ and a radius of 0.3 pc and R_{core} and C are 0.03 pc and 50 , which are typical respective values for the present sample, the mass–distance relationships with $\gamma = 1.0$ and 2.0 are indicated by the solid and dashed lines in Figure 12(a), respectively. As shown in Figure 12(a), the distribution of the upper limit of the core mass is roughly similar to the relationships expressed by the two lines. From this result, the mass (or the average H_2 density) of the core is suggested to depend on the H_2 density of the region where the core is formed in the clump, and the distribution of the core mass is suggested to be controlled by the H_2 density structure in the clump.

Figure 12(b) shows the ratio of the line width for the core and the clump plotted against the core distance. The starless cores with a high line width ratio (> 0.7) are concentrated in the center of the clump, and the upper limit of this ratio would gradually decrease with the core distance. The reason for this feature would be the change in both the core mass and the external pressure on the core surface.

Here, if we assume the cores are gravitationally

bound by the clump pressure, we can estimate the maximum line width of the cores using the virial equation (see § 4.1.2). If the clump with the physical parameters adopted in the above discussion is gravitationally bound, a line width of the clump is 2.2 km s^{-1} . In this case, the ratio of the maximum line width of the cores to the line width of the clump with $\gamma = 1.0$ and 2.0 is indicated by the solid and dashed lines, respectively, in Figure 12(b). As shown in Figure 12(b), the distribution of the upper limit of the line width ratio is similar to the relationships expressed by the two lines. As we have seen in § 4.1.2 and the above-mentioned mass–distance relationship, the external pressure on the core surface and the core mass are likely to depend on the core distance due to the H_2 density structure in the clump. Therefore, to bind gravitationally, the internal kinetic motion of the core would also necessarily depend on the core distance.

From the discussions in this subsection, we suggest that the central region of the clump, which has a density structure of $\sim R_{\text{cen}}^{-\gamma}$, is the environment in which the core with a large internal kinetic motion and a high average H_2 density is easily formed and that the internal kinetic motion and the average H_2 density of the core would depend on the H_2 density structure in the clump. In addition, according to the result in § 4.2.1, the mass of a star formed in the core would decrease with the distance from the center of the clump. Therefore, the physical characteristics of the cluster would depend on the H_2 density structure, internal kinetic motion, and the mechanism of core formation in the clump.

4.3. Mechanism of Cluster Formation

Finally, we discuss the relationship between cluster formation and the dense gas structures, cores and clumps. As we have seen in § 4.1 and § 4.2, many cores with a size of $\sim 0.03 \text{ pc}$ that are formed in a clump with a size of $\sim 0.3 \text{ pc}$ have a wide range of the line width and the mass, and the spatial distribution of the physical parameters of the cores would depend on the H_2 density structure in the clump. In addition, the mass of the star would depend mainly on the internal kinetic motion of the parental core. The stellar number density of the cluster is mentioned as an important characteristic of a cluster. The stellar number density of the cluster is generally much

higher than that of typical low-mass star-forming regions. In this regard, Saito et al. (2007) found a good relationship between the number density of YSOs associated with the clump and the average H_2 density of the clump, and they suggested that it is necessary for a clump to have a high average H_2 density for cluster formation to occur therein. This suggests that a relationship may exist between the number density of the cores in the clump and the average H_2 density of the clump. First, we estimated the number density of the cores to investigate this relationship.

Figure 13(a) shows the relationship between the number density of the cores in the clump, n_{core} , and the average H_2 density of the clump, $n(\text{H}_2)_{\text{clump}}$. A good correlation exists between the number density of the cores and the average H_2 density of the clump. This relationship is roughly expressed by the equation $n_{\text{core}} \sim n(\text{H}_2)_{\text{clump}}^{1.9}$ and the index of this relationship is similar to the index (~ 2.0) of the relationship between the number density of the YSOs and the average H_2 density of the clump obtained by Saito et al. (2007). This indicates that star formation in the clump is based on core formation in the clump. Although these relations are not expressed by the mechanism of core formation using simple gravitational instability as proposed by Saito et al. (2007), we suggest that for core formation with a high number density of the cores, it is necessary for the clump to have a high average H_2 density as an initial condition.

Next, we examine the relationship between the number of the cores and the YSOs to reveal the timescale of the cores. Figure 13(b) shows the number of YSOs, N_* , associated with the clump, which were identified by Saito et al. (2007), plotted against the number of cores in the clump, N_{core} . The numbers of the YSOs are one to three times larger than those of the cores. Considering that almost all of the YSOs would be low-mass stars, the lifetime of the YSO would be $\sim 1 \times 10^7 \text{ yr}$ (e.g., Lada 1999). In this case, the lifetime of the core is roughly estimated to be $\sim 3 \times 10^6 \text{ yr}$ if only one star is formed per core. In addition, we find 27 star-forming cores in this study and 10 in Saito et al. (2006), and the number corresponds to $\sim 19\%$ of all cores. This result indicates that the lifetime of the star-forming cores, which can be detected by our interferometric observation, is

$\sim 6 \times 10^5$ yr. This timescale is consistent with the fact that the typical mass of the cores associated with class II stars, whose lifetime is $\sim 10^6$ yr (e.g., Lada 1999), was roughly estimated to be $\ll 1M_\odot$ in low-mass star forming regions (e.g., Tsukagoshi et al. 2007) because the detection limit of the mass of the cores is $\sim 1M_\odot$. Therefore, most of the YSOs in the clump are not associated with the cores with a mass of $> 1M_\odot$ and the YSOs associated with these cores are regarded as young protostars.

Finally, we look at the core-formation efficiency (CFE) of the clump. Figure 13(c) shows CFEs ($\Sigma M_{\text{core}}/M_{\text{clump}}$, where M_{core} and M_{clump} are the mass of the core in the clump and the mass of the clump, respectively) plotted against the number density of cores in the clump. Although no strong correlation is seen between the CFEs and the number density of cores, the CFE gradually increases with the number density of cores in the clump. Considering the relationship between the number density of cores and the average H_2 density of the clump in Figure 13(a), this feature indicates that the dense gas in a clump with a high average H_2 density is efficiently converted into many cores. From the results that the CFE is $\sim 3\text{--}60\%$ and that the lifetime of the core is $\sim 3 \times 10^6$ yr in the above discussion, the conversion rate from the dense gas to cores per $\sim 1 \times 10^6$ yr (core-formation rate : CFR) in the clump is estimated to be $\sim 1 - 20\%/10^6$ yr. Thus, in a clump with a low average H_2 density, core formation with a low CFR (\sim a few $\%/10^6$ yr) could have occurred over a long time of $> 10^7$ yr if the CFR is always constant. However, only a part of the dense gas in the clump would be converted to cores because this timescale is longer than the typical lifetime of the GMC ($\sim 10^7$ yr; e.g., Blitz et al. 2007). On the contrary, in a clump with a high average H_2 density, core formation with a high CFR ($\geq 10\%/10^6$ yr) could have occurred over a short time of $\leq 10^7$ yr. This indicates that most of the dense gas in the clump would be converted to cores because this timescale is shorter than the typical lifetime of the GMC.

From the above considerations and the discussions in § 4.1 and 4.2, we determined that the mechanism of cluster formation would strongly depend on the mechanism of core formation in a clump and that the mechanism of core formation

would be controlled by both the H_2 density structure and the kinetic motion in the clump. Moreover, the characteristics of the cluster would be determined by the distribution of the physical parameters of cores in the clump. If a clump with a very high average H_2 density ($\sim 10^6 \text{ cm}^{-3}$), which has a size scale of ~ 0.3 pc, is formed in a GMC, this clump would be expected to form a cluster with a very high stellar number density very efficiently in a short time based on the discussion of the CFR. In addition, considering that the virial mass of the clump is similar to the LTE mass (Saito et al. 2007), the line width of the clump is estimated to be $\sim 10 \text{ km s}^{-1}$ using the average H_2 density and the radius. According to the line width–radius relationship in § 4.1.1 and the stellar mass–line width relationship in § 4.2.1, the cluster formed in the clump would include very massive (e.g., O3) stars. Thus, the clumps with a very high average H_2 density ($\sim 10^6 \text{ cm}^{-3}$) would be expected to form a cluster with both a very stellar number density and very massive stars. In addition, if many clumps are formed in a GMC, star-forming regions within the GMC will include many dense clusters with very massive stars and will be extended with a size of ~ 100 pc because the typical size of the GMC is ~ 100 pc. Indeed, very active star-forming regions occurring in external galaxies, for example, 30 Doradus region in LMC, are extended with a size scale of ≥ 100 pc and have many dense clusters, which contain many O3 stars, with a size scale of ~ 0.3 pc, for example, R136a core in 30 Doradus. Therefore, we suggest that the mechanism of cluster formation in such active star-forming regions would be basically similar to that in our galaxy, although the clumps in such active star-forming regions would have much higher H_2 density and much larger kinetic motion than those in our galaxy.

5. CONCLUSION

We made high-angular resolution observations with the Nobeyama Millimeter Array (NMA) of six cluster-forming regions including massive (proto)stars, in the $J = 1\text{--}0$ transition of C^{18}O molecular emission line and 98 GHz and 110 GHz continuum emission. We identified 171 C^{18}O cores in 12 clumps toward six cluster-forming regions including massive (proto)stars. Based on our observations, we studied the correlation between several

physical quantities of the C^{18}O cores and clumps, and discussed the formation mechanism of star clusters. The main results of the present study are summarized as follows:

1. The ranges of the radius, line width, and molecular mass of the cores are 0.01–0.09 pc, 0.43–3.33 km s^{-1} , and 0.5–54.1 M_{\odot} , respectively.

2. We identified 13 millimeter continuum sources (MCSs). Seven are associated with 2MASS sources and/or centimeter continuum sources (CCSs). Together with the one MCS that shows similar characteristics to the above seven MCSs, these eight MCSs would include massive protostars. The range of the mass of MCSs is 2.7–111 M_{\odot} . In addition, we compared C^{18}O cores with MCSs, 2MASS sources, and CCSs. We identified 27 star-forming cores including eight massive-star-forming cores.

3. Some cores have various line widths in a single clump. The range of the index of the relationship between the line width and radius of the core and the parental clump differs from core to core. This implies that the degree of dissipation of the turbulent motion varies within a single clump.

4. For most cores, the virial masses are about twice larger than the LTE masses. This indicates that external pressure is necessary for the cores to be gravitationally bound. Based on the virial analysis, the distribution of the external pressure required to bind the cores is likely to be comparable to that of the pressure in the clump with an H_2 density structure of $\sim r^{-\gamma}$ ($\gamma \sim 1\text{--}2$).

5. The mass of the cores increases with the line width. This indicates that the average H_2 density of the cores would depend on the kinetic motion of the dense gas in the core because the range of the radius of the core is small.

6. The mass of the star depends on the line width and the mass of the parental core. In addition, we found that the star-formation efficiency (SFE) is roughly constant at $\sim 50\%$ and that no clear dependence exists between the SFE and the mass of the formed stars.

7. The mass, line width, and external pressure of the core decrease with distance from the center of the clump, and a relationship exists between these decreases and the H_2 density structure of the clump. We suggest that the spatial distribution of physical parameters of the cores strongly depends

on the H_2 density structure in the clump.

8. The number density of the cores and the number density of the young (proto) stars in the clump have a similar relationship to the average H_2 density of the clump. In addition, the core-formation rate (CFR) of the clump is estimated to be $\sim 1\text{--}20\%$ per $\sim 1 \times 10^6$ yr and the CFR gradually increases with the average H_2 density of the clump.

We thank to the staff of the Nobeyama Radio Observatory (NRO) for both operating the Millimeter Array and helping us with data reduction. We thank to Kazuyoshi Sunada, Tomofumi Umemoto, and Takeshi Sakai and also to the referee for their valuable comments. This publication makes use of data produced by 2MASS, which is a joint project of the University of Massachusetts and Infrared Processing and Analysis Center funded by NASA and NSF. This study also made use of the SIMBAD database.

REFERENCES

- Bacmann, A., Lefloch, B., Ceccarelli, C., Castets, A., Steinacker, J. & Loinard, L. 2002, *A&A*, 389, L6
- Barsony, M. 1989, *ApJ*, 345, 268
- Bertoldi, F. & McKee, C. F. 1992, *ApJ*, 395, 140
- Bica, E., Dutra, C. M., & Barbuy, B. 2003, *A&A*, 397, 177
- Blitz, L., Fukui, Y., Kawamura, A., Leroy, A., Mizuno, N., & Rosolowsky, E. 2007, in *Protostars & Planets V*, ed. B. Reipurth, D. Jewitt & K. Keil (Tucson: Univ. Arizona Press), 951
- Carpenter, J. M., Snell, R. L., & Schloerb, F. P. 1990, *ApJ*, 362, 147
- Caselli, P., & Myers, P. C. 1995, *ApJ*, 446, 665
- Caselli, P., Walmsley, C. M., Tafalla, M., Dore, L., & Myers, P. C. 1999, *ApJ*, 523, L165
- Churchwell, E., Walmsley, C. M., & Wood, D. O. S. 1992, *A&A*, 253, 541
- Crampton, D., Georgelin, Y. M., & Georgelin, Y. P. 1978, *A&A*, 66, 1

- Eiroa, C., Casali, M. M., Miranda, L. F., & Ortiz, E. 1994, *A&A*, 290, 599
- Evans, N. J., II, & Blair, G. N. 1981, *ApJ*, 246, 394
- Felli, M., & Panagia, N. 1981, *A&A*, 102, 424
- Felli, M., Massi, F., Navarrini, A., Neri, R., Cesaroni, R., & Jenness, T. 2004, *A&A*, 420, 553
- Felli, M., Massi, F., Robberto, M., & Cesaroni, R. 2006, *A&A*, 453, 911
- Fontani, F., Cesaroni, R., Caselli, P., & Olmi, L. W. 2002, *A&A*, 389, 603
- Frerking, M. A., Langer, W. D., & Wilson, R. W. 1982, *ApJ*, 262, 590
- Gómez, Y., Garay, G., & Lizano, S. 1995, *ApJ*, 453, 727
- Hunter, T. R., Zhang, Q., & Sridharan, T. K. 2004, *ApJ*, 606, 929
- Kennicutt, R. C. 1984, *ApJ*, 287, 116
- Kurtz, S., Churchwell, E., & Wood, D. O. S. 1994, *ApJS*, 91, 659
- Lada, E. A. 1992, *ApJ*, 393, L25
- Lada, C. J. 1999, in *The Origin of Stars and Planetary Systems*, ed. C. J. Lada & N. D. Kylafis (Dordrecht: Kluwer), 143
- Lada, C. J., & Lada, E. A. 2003, *ARA&A*, 41, 57
- Larson, R. B. 1981, *MNRAS*, 194, 809
- Malumuth, E. M., & Heap, S. E. 1994, *AJ*, 107, 1054
- McKee, C. F., & Tan, J. C. 2003, *ApJ*, 585, 850
- Moffat, A. F. J., Fitzgerald, M. P., & Jackson, P. D. 1979, *A&AS*, 38, 197
- Momose, M., Ohashi, N., Kawabe, R., Nakano, T., & Hayashi, M. 1998, *ApJ*, 504, 314
- Olmi, L., Cesaroni, R., & Walmsley, C. M. 1993, *A&A*, 276, 489
- Onishi, T., Mizuno, A., Kawamura, A., Tachihara, K., & Fukui, Y. 2002, *ApJ*, 575, 950
- Panagia, N. 1973, *AJ*, 78, 929
- Panagia, N., & Felli, M. 1975 *A&A*, 39, 1
- Preibisch, Th., Osseukopf, V., Yorke, H. W., & Henning, Th. 1993, *A&A*, 279, 577
- Raboud, D., & Mermilliod, J.-A. 1998, *A&A*, 333, 897.
- Rohlfs, K., & Wilson, T. L. 2004, in *Tools of Radio Astronomy* (Berlin: Springer)
- Saito, H., Mizuno, N., Moriguchi, Y., Matunaga, K., Onishi, T., Mizuno, A., & Fukui, Y. 2001, *PASJ*, 53, 1037
- Saito, H., Saito, M., Moriguchi, Y., & Fukui, Y. 2006, *PASJ*, 58, 343
- Saito, H., Saito, M., Sunada, K., & Yonekura, Y. 2007, *ApJ*, 659, 459
- Schöier, F. L., Jørgensen, L. K., van Dishoeck, E. F., & Blake, G. A. 2004, *A&A*, 418, 185
- Sridharan, T. K., Beuther, H., Schilke, P., Menten, K. M., & Wyrowski, F. 2002, *ApJ*, 566, 931
- Tachihara, K., Onishi, T., Mizuno, A., & Fukui, Y. 2002, *A&A*, 385, 909
- Tukagoshi, T. 2007 preprint.
- Turner, K. C., & Terzian, Y. 1985, *AJ*, 90, 59
- Umemoto, T., Kamazaki, T., Sunada, K., Kitamura, Y., & Hasegawa, T. 2002, in the proceeding of the IAU 8th Asian-Pacific Regional Meeting, Volume II, ed. by S. Ikeuchi, & T. Hanawa, 229
- van der Tak, F. F. S., van Dishoeck, E. F., Evans, N. J., II, & Blake, G. A. 2000, *ApJ*, 537, 283
- van der Tak, F. F. S., Tuthill, P. G., & Danchi, W. C. 2005, *A&A*, 431, 993
- Wouterloot, J. G. A., & Brand, J. 1989, *A&AS*, 80, 149
- White, G. J., & Fridlund, C. V. M. 1992, *A&A*, 266, 452
- Zhang, Q., Hunter, T. R., Brand, J., Sridharan, T. K., Cesaroni, R., Molinari, S., Wang, J., & Kramer, M. 2005, *ApJ*, 625, 864

Zinchenko, I., Forsstroem, V., Lapinov, A., & Mattila, K. 1994, A&A, 288, 601

Zinchenko, I., Henning, Th., & Schreyer, K. 1997, A&AS, 124, 385

Zinchenko, I., Pirogov, L., & Toriseva, M. 1998, A&AS, 133, 337

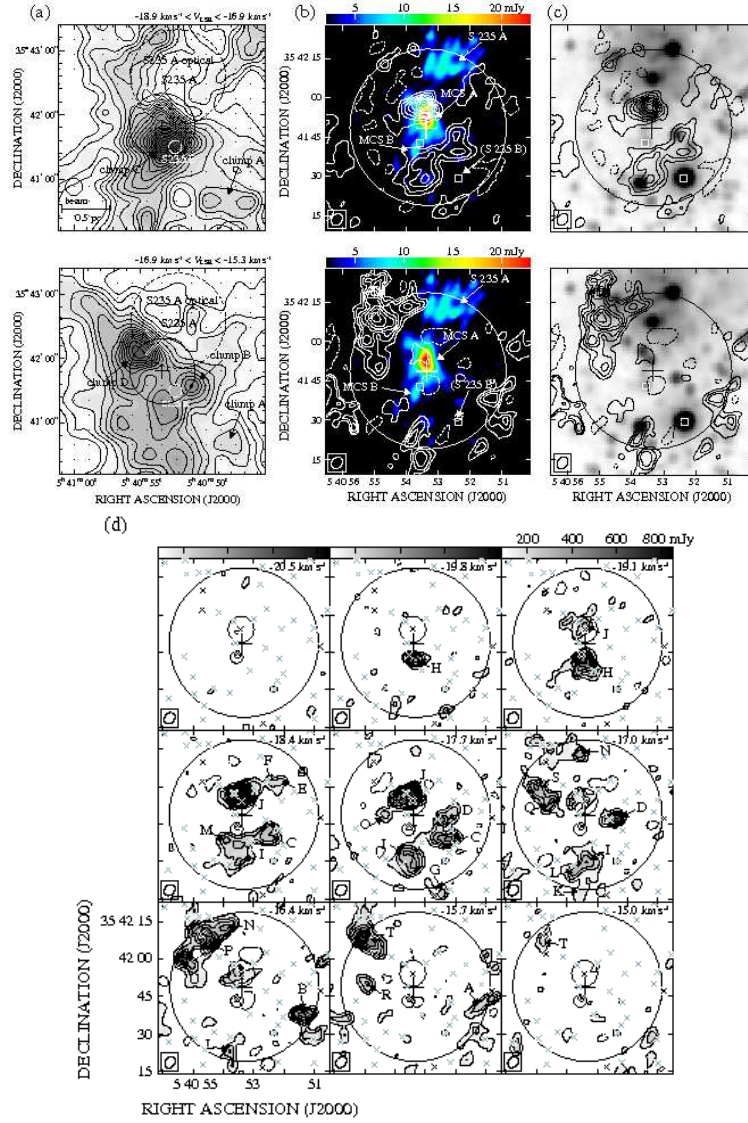


Fig. 1.— (a) The distribution of the C^{18}O ($J=1-0$) emission toward IRAS 05375+3540 and the clumps obtained by Saito et al. (2007) are shown. The integrated velocity ranges for the upper and lower panels are between -18.9 and -16.9 km s^{-1} and between -16.9 and -15.3 km s^{-1} , respectively. The large solid circle, the plus sign, and the squares denote the primary beam of NMA, the position of the maser source, and the CCS, respectively. The large cross and the dashed circles indicate the IRAS source and the H II region, respectively. (b) Color images of the 110 GHz continuum emission overlaid with contours of C^{18}O ($J=1-0$) emission obtained by the present observation. The integrated velocity is the same as in Figure 1(a). Contour levels are from -6σ in steps of 3σ , except for 0σ . The 1σ noise levels are 24 mJy for both panels. (c) Gray images of the 2MASS K_s band overlaid with contours of C^{18}O emission. (d) Channel maps of C^{18}O emission and the cores obtained by the present observation are shown. The LSR velocity is marked at the top right corner in each panel. The small circles and the crosses indicate the MCSs and 2MASS sources, respectively. In particular, the black crosses indicate the 2MASS source associated with the C^{18}O core. Contour levels are from -6σ in steps of 2σ and the 1σ noise levels are 34 mJy .

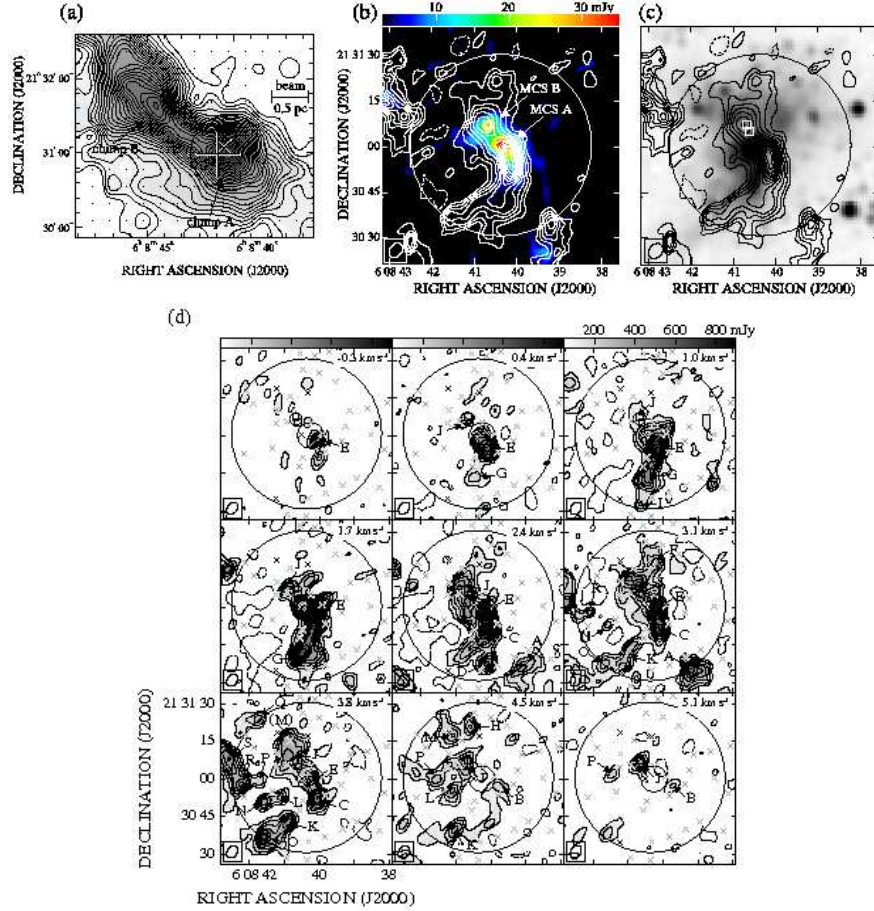


Fig. 2.— (a) Same as in Figure 1(a), but for IRAS 06056+2131. The integrated velocity range is between -1.5 and 6.5 km s^{-1} . (b) Same as in Figure 1(b), but the 1σ noise level is 12 mJy . (c) Same as in Figure 1(c). (d) Same as in Figure 1(d), but the 1σ noise levels are 30 mJy .

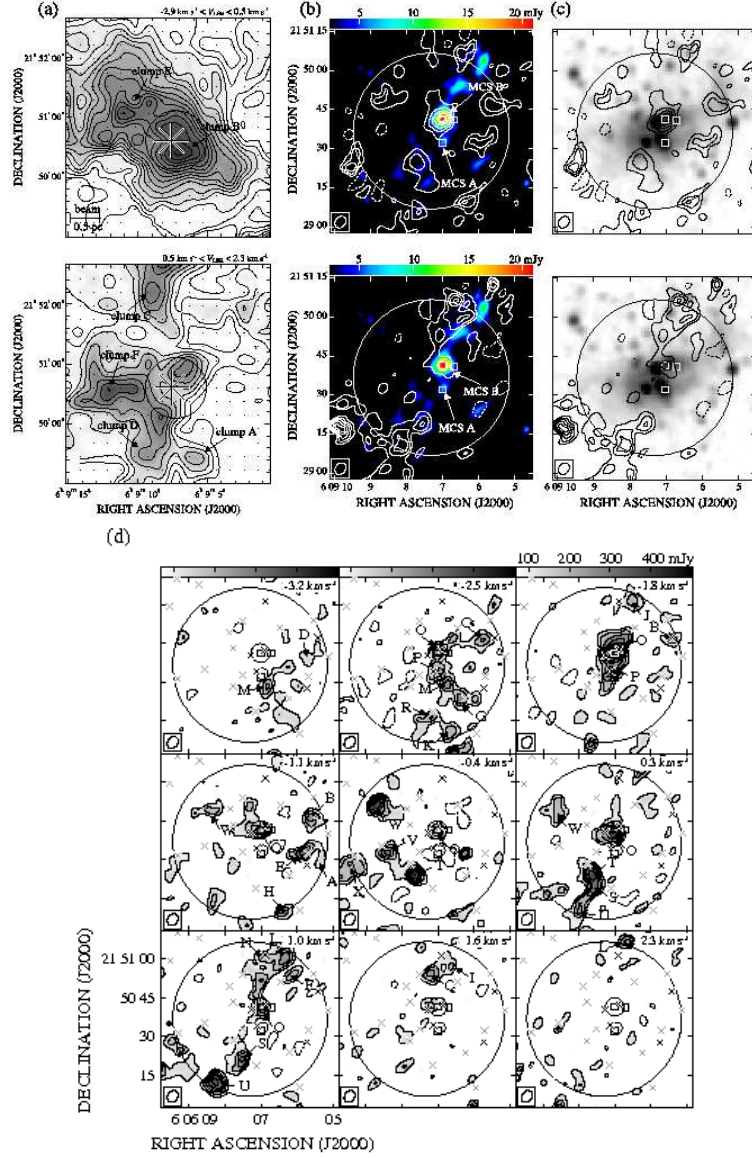


Fig. 3.— (a) Same as in Figure 1(a), but for IRAS 06061+2151. The integrated velocity ranges for the upper and lower panels are between -2.9 and 0.5 km s^{-1} and between 0.5 and 2.3 km s^{-1} , respectively. (b) Same as in Figure 1(b), but the 1σ noise levels are 18 mJy (upper panel) and 21 mJy (lower panel). (c) Same as in Figure 1(c). (d) Same as in Figure 1(d), but the 1σ noise levels are 30 mJy.

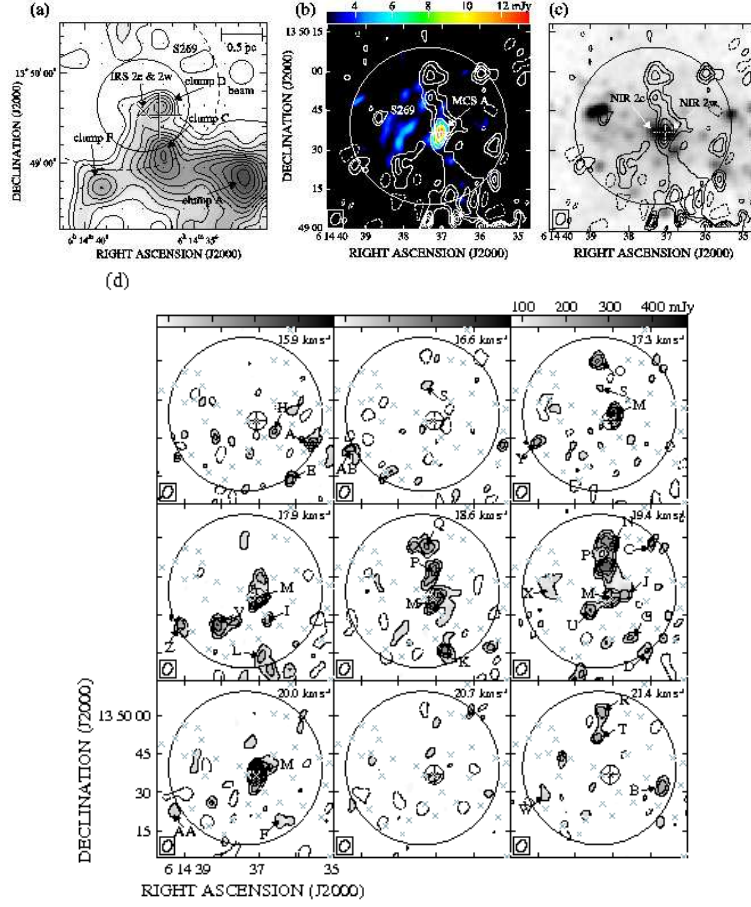


Fig. 4.— (a) Same as in Figure 1(a), but for IRAS 06117+1350. The integrated velocity range is between 14.5 and 23.0 km s⁻¹. The cross indicates NIR 2e & 2w. (b) Same as in Figure 1(b), but the color image is of the 98 GHz continuum emission and the 1 σ noise level is 10 mJy. (c) Same as in Figure 1(c). (d) Same as in Figure 1(d), but the 1 σ noise levels are 30 mJy.

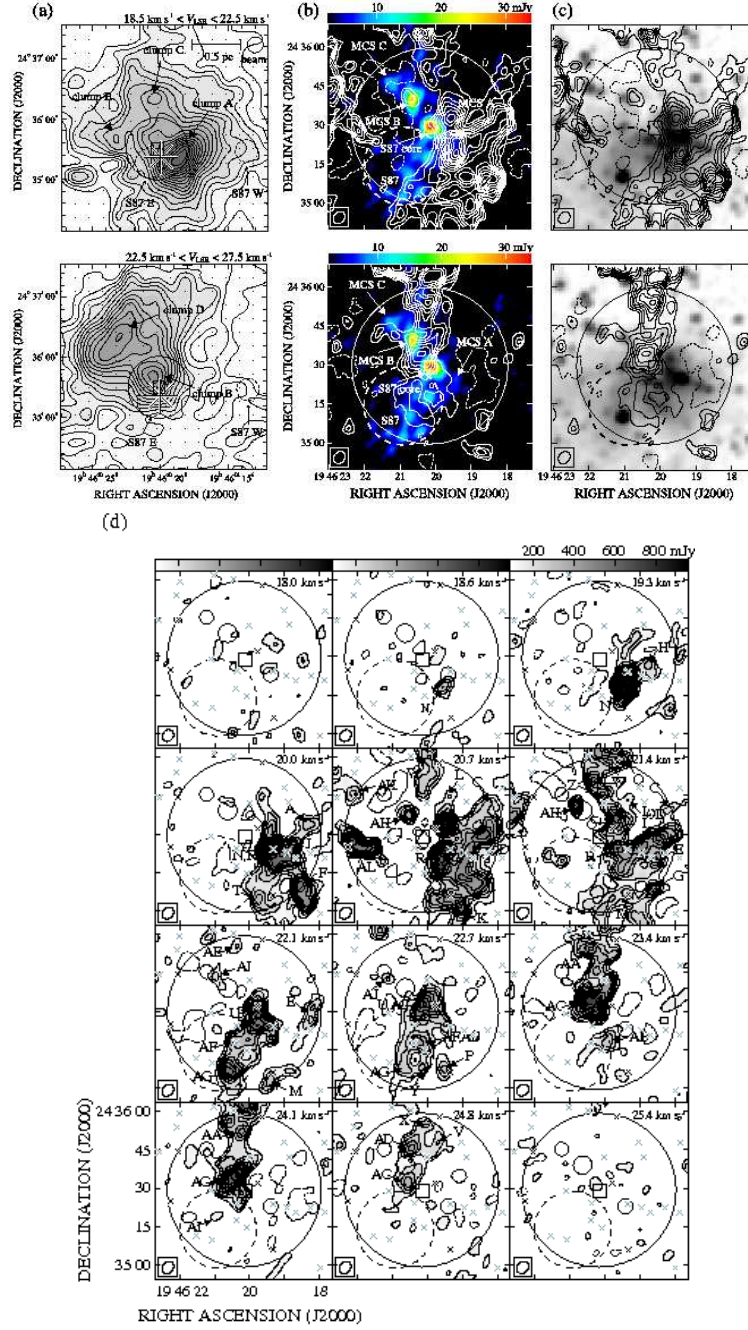


Fig. 5.— (a) Same as in Figure 1(a), but for IRAS 19442+2427. The dashed circles denote the area of the radio H II regions. The integrated velocity ranges for the upper and lower panels are between 18.5 and 22.5 km s^{-1} and between 22.5 and 27.5 km s^{-1} , respectively. (b) Same as in Figure 1(b), but the 1σ noise levels are 14 mJy (upper panel) and 12 mJy (lower panel). (c) Same as in Figure 1(c). (d) Same as in Figure 1(d), but the 1σ noise levels are 30 mJy.

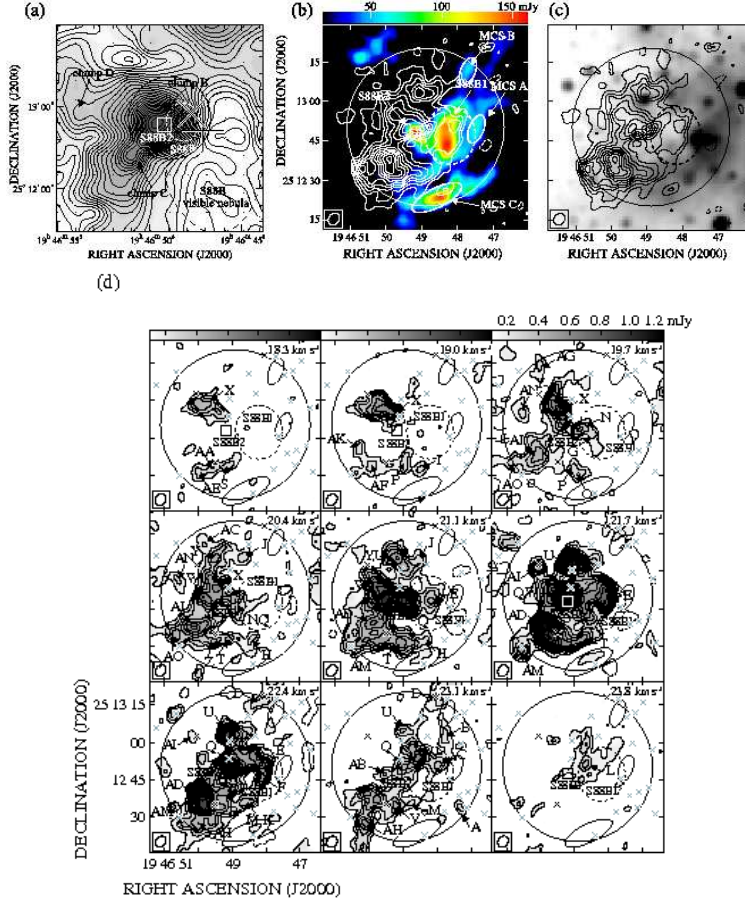


Fig. 6.— (a) Same as in Figure 1(a), but for IRAS 19446+2505. The integrated velocity range is between 16.5 and 26.5 km s⁻¹. The square and the dashed circle denote the area of the radio H II regions S88 B1 and B2, respectively. The dashed curved line denotes the boundary of the optical H II regions S88 B. (b) Same as in Figure 1(b), but the color image is of the 98 GHz continuum emission and the 1 σ noise level is 13 mJy. (c) Same as in Figure 1(c). (d) Same as in Figure 1(d), but the 1 σ noise levels are 40 mJy.

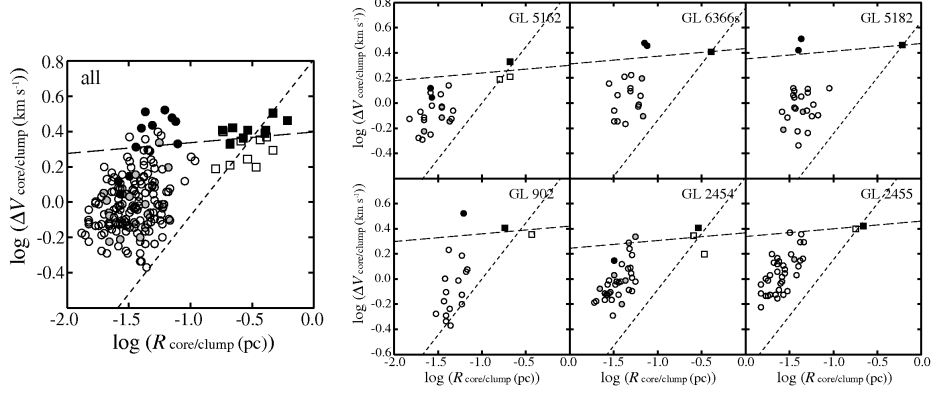


Fig. 7.— The correlation between the radius and the line width of the cores and the clumps. The circles indicate the cores identified in this paper and by Saito et al. (2006). The squares indicate the clumps identified by Saito et al. (2007). The white, gray, and black symbols indicate the objects without 2MASS sources, those with 2MASS sources, and those with massive stars, respectively. The long- and short-dashed lines indicate the relationships of $\Delta V \sim R^{0.06}$ and $\Delta V \sim R^{0.89}$ using the average line width and the average radius of the clumps in each panel, respectively

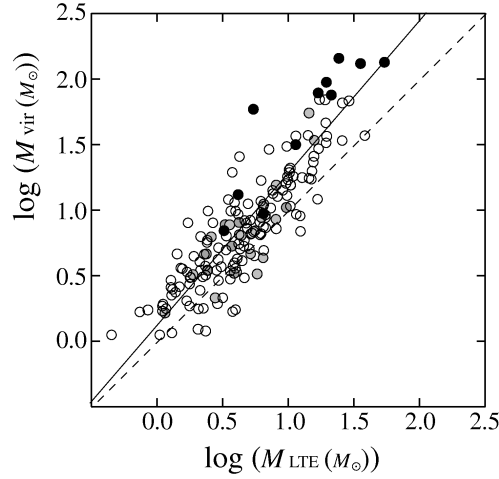


Fig. 8.— Virial mass plotted against the LTE mass for all cores. The symbols are the same as in Figure 7. The dashed line indicates the relationship of $M_{\text{vir}} = M_{\text{LTE}}$. The solid line denotes the best fit power-law relationship for all cores except for those associated with massive (proto)stars, $M_{\text{vir}} = 1.5 \times M_{\text{LTE}}^{1.1}$.

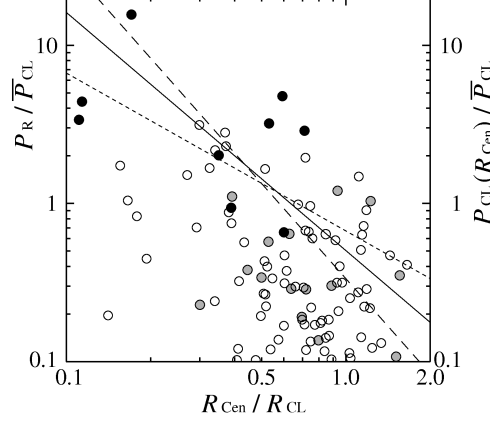


Fig. 9.— The ratio of the required pressure to the average clump pressure plotted against the distance from the center of the clump for all cores with a virial ratio of > 1 . The dotted, solid, and dashed lines indicate the distribution of the clump pressure with the H_2 density structure of $n(\text{H}_2) \propto (R_{\text{Cen}}/R_{\text{CL}})^{-1.0}$, $\propto (R_{\text{Cen}}/R_{\text{CL}})^{-1.5}$, and $\propto (R_{\text{Cen}}/R_{\text{CL}})^{-2.0}$, respectively. The symbols are the same as in Figure 7.

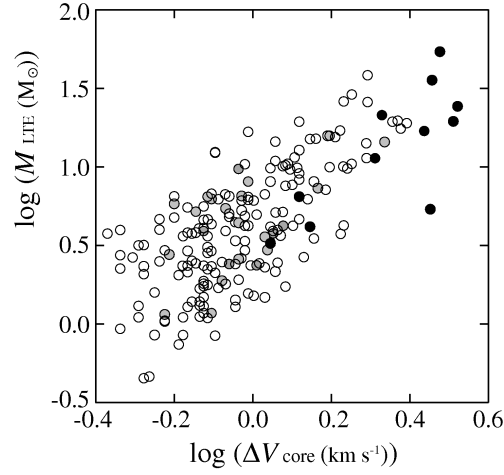


Fig. 10.— The LTE mass plotted against the line width of the cores. The symbols are the same as in Figure 7.

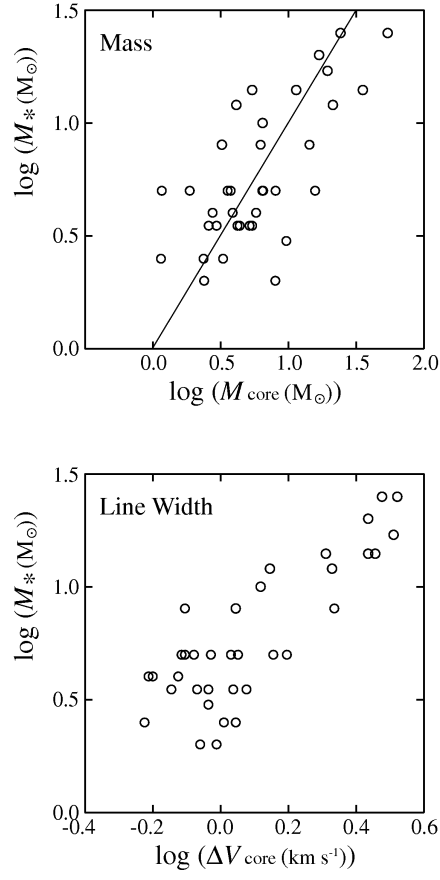


Fig. 11.— The mass of associated stars plotted against the LTE mass and the line width of the star-forming cores. The solid line indicates the relationship of $M_* = M_{\text{core}}$.

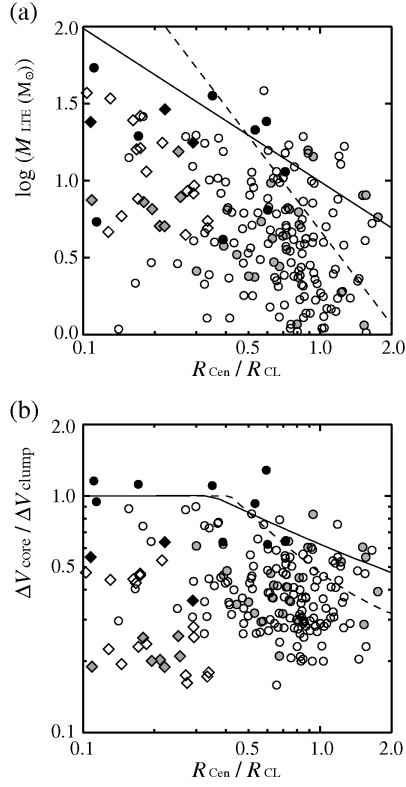


Fig. 12.— (a) The LTE mass of the cores plotted against the distance from the center of the clump for all cores. The solid and dashed lines indicate the relationship of $M_{\text{core}} \propto n_0 (R_{\text{Cen}}/R_{\text{CL}})^{-\gamma}$, with $\gamma = 1.0$ and 2.0 , respectively. (b) The ratio of the line width for the cores and the clump plotted against the distance from the center of the clump for all cores. The lines indicate the relationship between the maximum ratio of the line width for the cores and the clump and the distance from the center of the clump when the mass of the core has the same relationships as in Figure 12(a). The solid and dashed lines indicate this relationship with $\gamma = 1.0$ and 2.0 , respectively. The symbols are the same as in Figure 7.

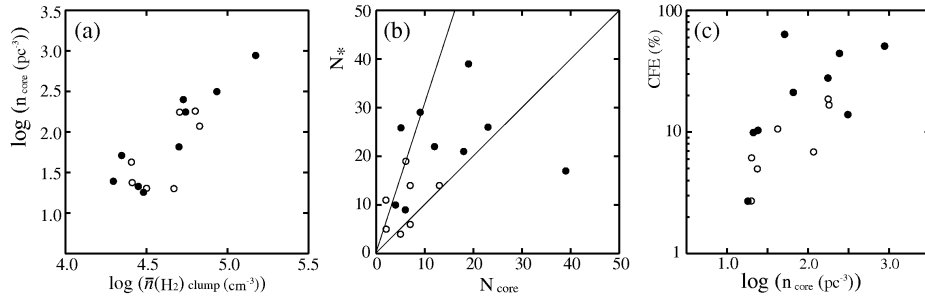


Fig. 13.— (a) The number density of the cores in each clump plotted against the average H_2 density of the clump. (b) The correlation between the number of cores and the number of associated stars in each clump. The solid lines indicate the relationships of $N_* = N_{\text{core}}$ and $N_* = 3 \times N_{\text{core}}$, respectively. (c) Correlation diagram of CFE against the number density of the cores in each clump. The open and filled circles indicate clumps without and with massive star formation, respectively.

Table 1: Observation targets.

Object	Position(J2000)						Distance (kpc)	L_{IRAS} ($10^4 L_{\odot}$)	cluster	CCS ^a	Ref. ^b
	α (h m s)			δ ($^{\circ}$ ' ")							
IRAS 05375+3540	05	40	53.6	35	42	16	1.8	2.5	GL 5162	S235A–B	1
IRAS 06056+2131	06	08	41.0	21	31	01	3.5	7.2	GL 6366s	weak emission	2
IRAS 06061+2151	06	09	07.8	21	50	39	3.5	3.4	GL 5182	weak emission	2
IRAS 06117+1350	06	14	36.6	13	49	35	3.8	6.5	GL 902	S269	3
IRAS 19442+2427	19	46	19.9	24	35	24	2.3	5.0	GL 2454	S87	4
IRAS 19446+2505	19	46	47.0	25	12	43	2.0	13.0	GL 2455	S88B1,S88B2	4

^a CCS means the centimeter continuum source.^b Data used for the distance of the target.

References. —(1) Evans & Blair 1981; (2) Moffat et al. 1979; (3) Wouterloot & Brand 1989; (4) Crampton et al. 1978.

Table 2: Beams and RMS noise for NMA Observations.

Object	field center		Line or Continuum	beam		r.m.s. (mJy beam ⁻¹)
	α (J2000) (h m s)	δ (J2000) ($^{\circ}$ ' ")		size ($'' \times ''$)	P.A. ($^{\circ}$)	
IRAS 05375+3540	05 40 53.3	35 41 48.8	98 GHz cont.	5.2×4.2	-34	0.79
			110 GHz cont.	4.7×3.8	-36	0.97
			C ¹⁸ O	4.7×3.8	-65	110 ^a
IRAS 06056+2131	06 08 40.4	21 31 00.6	98 GHz cont.	5.6×4.4	-37	0.78
			110 GHz cont.	5.0×3.9	-37	1.08
			C ¹⁸ O	5.0×3.9	-38	80 ^a
IRAS 06061+2151	06 09 07.3	21 50 36.7	98 GHz cont.	5.4×4.3	-39	0.61
			110 GHz cont.	4.9×3.8	-39	0.93
			C ¹⁸ O	4.9×3.8	-29	78 ^a
IRAS 06117+1350	06 14 47.2	13 49 39.3	98 GHz cont.	5.2×3.8	-23	0.58
			110 GHz cont.	4.6×3.4	-24	0.95
			C ¹⁸ O	4.6×3.4	-28	63 ^a
IRAS 19442+2427	19 46 20.1	24 35 29.4	98 GHz cont.	5.3×4.4	-40	0.77
			110 GHz cont.	4.8×3.9	-40	0.80
			C ¹⁸ O	4.8×3.9	-41	80 ^a
IRAS 19446+2505	19 46 47.0	25 12 43.2	98 GHz cont.	5.4×4.4	-39	3.6
			110 GHz cont.	4.9×4.0	-39	6.5
			C ¹⁸ O	4.9×4.0	-37	84 ^a

^a The RMS noises are the value per 1 channel (31.25 kHz).

TABLE 3
OBSERVED PROPERTIES OF C¹⁸O CORES.

Region	core	Position ^a		T_R^* ^b (K)	V_{LSR} ^b (km s ⁻¹)	ΔV ^b (km s ⁻¹)	ΔV_{com} ^c (km s ⁻¹)	$\int T_R^* dV$ (K km s ⁻¹)
		α (J2000) (h m s)	δ (J2000) (^o ' ")					
IRAS 05375+3540	core A	05 40 51.3	35 41 40	2.0	-15.9	0.85	0.92	1.7
	core B	05 40 51.3	35 41 37	3.0	-16.3	0.87	0.96	2.6
	core C	05 40 52.3	35 41 39	2.1	-18.0	1.09	1.18	2.3
	core D	05 40 52.4	35 41 47	2.5	-17.3	0.89	0.85	2.2
	core E	05 40 52.4	35 42 02	1.5	-18.2	0.51	0.56	0.8
	core F	05 40 52.4	35 41 59	1.3	-18.7	0.49	0.53	0.7
	core G	05 40 52.8	35 41 18	2.4	-17.1	0.53	0.60	1.3
	core H	05 40 53.4	35 41 41	2.3	-19.4	1.14	1.11	2.7
	core I	05 40 53.4	35 41 29	2.7	-17.8	1.33	1.38	3.8
	core J	05 40 53.4	35 41 56	5.1	-18.2	1.21	1.31	6.6
	core K	05 40 53.6	35 41 17	2.7	-16.7	0.68	0.77	1.9
	core L	05 40 53.8	35 41 25	2.0	-16.8	0.70	0.75	1.5
	core M	05 40 53.9	35 41 40	2.5	-18.8	0.58	0.75	1.6
	core N	05 40 54.2	35 42 13	2.5	-16.6	0.87	0.87	2.4
	core O	05 40 54.2	35 41 49	1.4	-17.3	0.51	0.55	0.8
	core P	05 40 54.4	35 42 08	4.0	-16.3	0.89	0.94	3.9
	core Q	05 40 54.5	35 41 55	1.9	-16.9	0.67	0.73	1.3
	core R	05 40 54.9	35 41 49	1.4	-15.8	1.23	1.21	1.8
	core S	05 40 55.0	35 41 58	3.3	-16.7	0.72	0.72	2.5
	core T	05 40 55.0	35 42 09	5.9	-15.9	0.70	0.77	4.4
	core U	05 40 55.3	35 42 02	3.2	-16.3	0.41	0.51	1.4
IRAS 06056+2131	core A	06 08 39.1	21 30 35	4.7	2.8	0.87	0.97	4.1
	core B	06 08 39.8	21 30 58	0.9	4.5	1.11	1.16	1.1
	core C	06 08 40.1	21 30 52	2.9	2.6	1.36	1.62	4.0
	core D	06 08 40.1	21 30 38	2.7	2.4	1.09	1.25	3.0
	core E	06 08 40.2	21 30 59	3.3	2.4	2.81	3.00	9.5
	core F	06 08 40.2	21 31 18	1.6	2.9	0.92	0.94	1.5
	core G	06 08 40.5	21 30 43	2.7	1.6	1.55	1.67	4.5
	core H	06 08 40.6	21 31 17	1.4	4.4	0.67	0.72	1.0
	core I	06 08 40.6	21 30 33	1.3	0.9	0.90	0.84	1.2
	core J	06 08 40.8	21 31 07	1.5	3.1	3.89	2.87	6.0
	core K	06 08 41.0	21 30 41	1.8	3.6	1.40	1.57	2.6
	core L	06 08 41.1	21 30 55	1.3	4.1	0.63	0.68	0.9
	core M	06 08 41.1	21 31 17	1.4	4.3	0.68	0.78	1.0
	core N	06 08 41.6	21 30 50	1.9	3.6	0.65	0.68	1.2
	core O	06 08 41.6	21 30 37	3.2	3.6	1.14	1.31	3.6
	core P	06 08 41.7	21 31 00	1.1	4.3	1.36	1.43	1.6
	core Q	06 08 41.8	21 31 24	2.3	3.8	0.68	0.72	1.5
	core R	06 08 42.2	21 30 59	2.6	3.8	0.84	0.87	2.2
	core S	06 08 42.4	21 31 04	2.6	3.6	1.11	1.14	3.0
IRAS 06061+2151	core A	06 09 05.3	21 50 32	1.1	-1.3	0.51	1.11	0.6
				2.0	-0.6	0.53	—	1.1
	core B	06 09 05.6	21 50 46	1.8	-1.1	0.84	0.92	1.5
	core C	06 09 05.8	21 50 47	1.6	-2.3	0.46	0.46	0.8
	core D	06 09 05.8	21 50 42	1.2	-3.4	1.04	1.13	1.3
	core E	06 09 05.9	21 50 32	1.8	-1.2	0.82	0.85	1.5
	core F	06 09 06.3	21 50 53	1.5	0.3	0.82	0.87	1.3
	core G	06 09 06.4	21 50 24	1.3	-2.4	0.84	0.90	1.1
	core H	06 09 06.4	21 50 10	1.9	-0.9	0.99	1.02	1.9
	core I	06 09 06.4	21 50 55	1.8	1.2	0.77	0.78	1.4
	core J	06 09 06.5	21 51 01	1.5	-1.7	0.61	0.58	1.0
	core K	06 09 06.6	21 50 11	1.6	-2.4	0.58	0.60	0.9
	core L	06 09 06.7	21 51 06	1.9	2.3	0.84	0.85	1.6
	core M	06 09 06.9	21 50 31	1.0	-2.6	1.21	1.26	1.4
	core N	06 09 07.0	21 51 01	1.8	0.7	0.53	0.61	0.9

TABLE 3—*Continued*

Region	core	Position ^a		T_{R}^* ^b (K)	V_{LSR}^b (km s ⁻¹)	ΔV^b (km s ⁻¹)	ΔV_{com}^c (km s ⁻¹)	$\int T_{\text{R}}^* dV$ (K km s ⁻¹)
		$\alpha(\text{J2000})$ (h m s)	$\delta(\text{J2000})$ (° ' ")					
	core O	06 09 07.0	21 50 41	2.4	-1.9	1.04	3.24	2.6
				0.9	-0.7	0.85	—	0.8
				1.8	0.3	1.19	—	2.3
				0.6	1.7	0.68	—	0.4
				0.5	2.6	0.60	—	0.3
	core P	06 09 07.1	21 50 38	1.3	-1.8	1.25	2.73	1.6
				0.8	0.5	0.51	—	0.6
	core Q	06 09 07.2	21 50 54	1.6	1.3	0.92	0.97	1.5
	core R	06 09 07.2	21 50 17	1.5	-2.2	0.72	0.77	1.1
	core S	06 09 07.6	21 50 19	2.1	0.7	1.23	1.30	2.7
	core T	06 09 07.7	21 50 24	2.4	0.0	1.28	1.31	3.0
	core U	06 09 08.1	21 50 11	3.2	0.7	0.77	0.80	2.5
	core V	06 09 08.4	21 50 33	1.3	-0.5	0.99	1.16	1.3
	core W	06 09 08.6	21 50 52	2.3	-0.3	1.14	1.21	2.7
	core X	06 09 09.3	21 50 24	2.1	-0.3	1.26	1.31	2.9
IRAS 06117+1350	core A	06 14 35.6	13 49 28	2.0	15.7	0.70	0.77	1.4
	core B	06 14 35.7	13 49 31	1.8	21.4	0.94	1.01	1.8
	core C	06 14 36.0	13 49 58	2.0	19.2	0.46	0.67	0.9
	core D	06 14 36.1	13 49 16	1.5	19.4	0.60	0.70	0.9
	core E	06 14 36.2	13 49 14	2.9	15.8	0.44	0.46	1.3
	core F	06 14 36.4	13 49 17	2.6	19.6	0.44	0.46	1.1
	core G	06 14 36.5	13 49 22	1.5	19.5	0.65	0.68	1.0
	core H	06 14 36.6	13 49 32	1.0	15.8	0.67	0.75	0.7
	core I	06 14 36.7	13 49 28	1.9	17.7	0.49	0.53	0.9
	core J	06 14 36.7	13 49 38	1.0	19.6	1.45	1.54	1.5
	core K	06 14 36.8	13 49 16	1.6	18.5	0.75	0.78	1.2
	core L	06 14 36.9	13 49 14	1.7	17.9	0.68	0.75	1.1
	core M	06 14 37.0	13 49 36	1.7	17.6	0.72	3.33	1.3
				1.5	18.7	0.77	—	1.2
				2.2	20.2	1.06	—	2.5
	core N	06 14 37.0	13 49 57	2.4	19.4	0.55	0.63	1.4
	core O	06 14 37.1	13 50 00	1.9	17.4	0.53	0.51	1.0
	core P	06 14 37.2	13 49 49	1.9	19.1	1.11	1.14	2.2
	core Q	06 14 37.3	13 49 57	1.4	18.5	0.89	0.97	1.2
	core R	06 14 37.3	13 50 02	2.5	21.6	0.51	0.58	1.4
	core S	06 14 37.4	13 49 50	1.1	16.9	0.61	0.56	0.7
	core T	06 14 37.4	13 49 51	1.6	21.3	0.46	0.53	0.7
	core U	06 14 37.6	13 49 32	1.4	19.3	0.51	0.53	0.8
	core V	06 14 38.1	13 49 26	1.6	17.8	0.51	1.19	0.9
				1.5	18.5	0.60	—	1.0
	core W	06 14 38.8	13 49 28	2.3	21.7	0.48	0.49	1.1
	core X	06 14 38.8	13 49 39	0.8	19.2	1.62	1.71	1.3
	core Y	06 14 39.0	13 49 28	1.7	17.1	0.60	0.58	1.0
	core Z	06 14 39.1	13 49 27	2.5	18.0	0.43	0.43	1.1
	core AA	06 14 39.2	13 49 25	3.0	20.4	0.60	0.63	1.9
	core AB	06 14 39.2	13 49 26	2.5	16.7	0.63	0.70	1.6
IRAS 19442+2427	core A	19 46 18.2	24 35 34	2.4	20.4	0.67	0.75	1.6
	core B	19 46 18.2	24 35 41	1.6	27.1	0.53	0.51	0.9
	core C	19 46 18.3	24 35 41	2.4	20.9	0.73	0.77	1.8
	core D	19 46 18.4	24 35 30	3.6	21.0	1.21	1.31	4.4
	core E	19 46 18.4	24 35 03	3.3	21.5	0.72	0.82	2.3
	core F	19 46 18.5	24 35 09	6.1	20.3	0.72	0.80	4.3
	core G	19 46 18.6	24 35 09	2.6	21.5	0.61	0.68	1.6
	core H	19 46 18.7	24 35 26	2.3	19.6	0.77	0.75	1.8
	core I	19 46 18.8	24 35 25	4.5	21.1	0.89	0.96	4.0

TABLE 3—*Continued*

Region	core	Position ^a		T_{R}^* ^b (K)	V_{LSR}^b (km s ⁻¹)	ΔV^b (km s ⁻¹)	ΔV_{com}^c (km s ⁻¹)	$\int T_{\text{R}}^* dV$ (K km s ⁻¹)
		$\alpha(\text{J2000})$ (h m s)	$\delta(\text{J2000})$ (° ' ")					
	core J	19 46 18.8	24 35 21	3.8	20.4	1.06	1.11	4.1
	core K	19 46 19.1	24 35 03	4.4	20.6	0.84	0.96	3.7
	core L	19 46 19.2	24 35 44	1.3	21.3	0.84	0.80	1.1
	core M	19 46 19.3	24 35 04	1.6	21.5	0.72	1.07	1.2
				1.2	22.1	0.67	—	0.8
	core N	19 46 19.3	24 35 19	4.6	19.8	1.31	1.55	6.2
	core O	19 46 19.4	24 35 33	3.7	20.8	0.84	0.97	3.1
	core P	19 46 19.5	24 35 07	1.4	22.9	0.82	0.90	1.1
	core Q	19 46 19.5	24 35 59	2.9	21.3	0.89	0.94	2.5
	core R	19 46 19.6	24 35 17	3.5	20.9	1.04	1.23	3.8
	core S	19 46 19.6	24 35 56	2.5	27.1	0.44	0.46	1.1
	core T	19 46 19.7	24 35 04	2.5	20.1	1.01	0.96	2.6
	core U	19 46 19.7	24 35 31	1.7	21.5	1.06	2.17	1.8
				2.3	22.3	1.14	—	2.7
	core V	19 46 19.8	24 35 43	1.3	24.7	0.61	0.68	0.8
	core W	19 46 19.9	24 35 59	4.3	20.8	0.94	0.97	4.1
	core X	19 46 20.0	24 35 56	1.5	24.9	0.78	0.90	1.2
	core Y	19 46 20.1	24 35 08	1.6	22.7	0.65	0.67	1.1
	core Z	19 46 20.2	24 35 51	2.8	21.1	0.78	0.75	2.2
	core AA	19 46 20.2	24 35 53	3.2	23.8	1.64	1.74	5.4
	core AB	19 46 20.3	24 35 18	2.1	22.9	0.97	1.02	2.0
	core AC	19 46 20.4	24 35 34	6.8	23.7	1.81	1.94	12.2
	core AD	19 46 20.4	24 35 46	2.3	24.7	0.70	0.78	1.6
	core AE	19 46 20.4	24 35 53	2.4	21.5	0.73	0.77	1.8
	core AF	19 46 20.5	24 35 19	1.7	22.1	0.99	1.07	1.6
	core AG	19 46 20.6	24 35 06	3.3	23.6	1.13	1.21	3.8
	core AH	19 46 20.7	24 35 41	2.3	21.2	1.14	1.40	2.8
	core AI	19 46 20.8	24 35 20	1.2	24.3	0.65	0.67	0.8
	core AJ	19 46 21.1	24 35 42	1.4	23.2	0.58	0.65	0.8
	core AK	19 46 22.0	24 35 46	2.3	20.7	0.77	0.84	1.8
	core AL	19 46 22.1	24 35 28	6.3	20.8	0.53	0.63	3.3
IRAS 19446+2505	core A	19 46 47.3	25 12 34	1.8	22.4	0.60	0.60	1.1
	core B	19 46 47.7	25 13 04	1.5	22.0	0.84	0.92	1.2
	core C	19 46 47.9	25 12 51	1.7	22.0	0.63	0.73	1.1
	core D	19 46 47.9	25 13 17	1.6	21.8	1.74	1.79	2.9
	core E	19 46 48.0	25 12 52	4.2	21.0	1.35	1.40	5.9
	core F	19 46 48.1	25 12 46	1.9	21.7	0.73	0.73	1.4
	core G	19 46 48.1	25 12 47	1.2	18.8	0.77	0.75	1.0
	core H	19 46 48.3	25 12 33	1.3	19.8	0.67	0.75	0.9
	core I	19 46 48.5	25 12 32	1.4	18.1	0.61	0.73	0.8
	core J	19 46 48.5	25 13 05	1.6	19.9	0.67	0.70	1.1
	core K	19 46 48.6	25 12 37	2.4	21.2	0.87	0.96	2.1
	core L	19 46 48.6	25 12 53	2.6	22.2	1.13	1.26	3.0
	core M	19 46 48.7	25 12 36	1.4	22.0	0.73	0.82	1.0
	core N	19 46 48.7	25 12 50	1.4	18.8	0.82	0.90	1.1
	core O	19 46 48.8	25 12 30	1.7	18.8	0.78	0.75	1.3
	core P	19 46 48.9	25 12 34	1.5	18.4	0.92	1.04	1.5
	core Q	19 46 48.9	25 12 49	4.8	20.9	2.29	2.34	11.4
	core R	19 46 49.0	25 12 41	2.5	21.3	1.09	1.19	2.8
	core S	19 46 49.1	25 12 34	1.7	17.6	0.56	0.60	1.0
	core T	19 46 49.1	25 12 31	3.3	20.6	1.54	1.57	5.2
	core U	19 46 49.1	25 13 04	6.2	21.0	1.23	1.28	7.9
	core V	19 46 49.2	25 12 34	2.6	21.8	1.25	1.31	3.4
	core W	19 46 49.3	25 12 50	4.9	20.5	1.86	1.96	9.9
	core X	19 46 49.4	25 12 56	3.3	18.6	2.15	2.27	7.4
	core Y	19 46 49.4	25 13 06	2.6	20.0	1.13	1.07	3.1

TABLE 3—*Continued*

Region	core	Position ^a		T_R^* ^b (K)	V_{LSR} ^b (km s ⁻¹)	ΔV ^b (km s ⁻¹)	ΔV_{com} ^c (km s ⁻¹)	$\int T_R^* dV$ (K km s ⁻¹)
		$\alpha(J2000)$ (h m s)	$\delta(J2000)$ (^o ' ")					
	core Z	19 46 49.5	25 12 32	2.1	19.5	0.73	0.77	1.7
	core AA	19 46 49.5	25 12 33	1.7	17.6	0.68	0.78	1.3
	core AB	19 46 49.5	25 12 47	1.7	22.0	0.70	0.77	1.2
	core AC	19 46 49.7	25 13 11	1.4	19.4	1.07	1.14	1.5
	core AD	19 46 49.8	25 12 39	6.8	21.3	1.83	1.96	12.8
	core AE	19 46 49.9	25 12 31	2.0	17.6	0.94	1.07	2.0
	core AF	19 46 49.9	25 12 34	1.7	18.2	0.77	0.80	1.3
	core AG	19 46 49.9	25 13 14	1.7	18.9	1.28	1.35	2.2
	core AH	19 46 50.0	25 12 28	4.9	21.8	0.97	1.11	5.0
	core AI	19 46 50.0	25 13 02	2.7	20.8	0.99	1.09	2.8
	core AJ	19 46 50.1	25 12 38	3.6	19.4	1.35	1.45	4.9
	core AK	19 46 50.2	25 12 40	1.4	18.2	0.99	0.97	1.4
	core AL	19 46 50.3	25 12 43	1.3	16.7	0.97	1.01	1.2
	core AM	19 46 50.5	25 12 28	3.9	20.8	1.42	1.47	5.7
	core AN	19 46 50.5	25 12 56	1.7	19.1	1.70	1.71	2.8
	core AO	19 46 50.6	25 12 35	3.2	19.4	1.33	1.38	4.4

^aThe position of the integrated intensity peak of C¹⁸O cores.

^bThe parameters are derived from a Gaussian fitting for the line profile at the integrated intensity peak of C¹⁸O cores.

^cThe line width of composite spectrum made using the data within the cores.

Table 4: Observed properties of MCSs and HII regions.

Region	total flux ^a		name	Position ^b		total flux		F.F. ^c (mJy)
	98 GHz (mJy)	110 GHz (mJy)		$\alpha(J2000)$ (h m s)	$\delta(J2000)$ (^o ' ")	98 GHz (mJy)	110 GHz (mJy)	
IRAS 05375+3540	263±7.0	258±9.2	MCS A	05 40 53.4	35 41 53	31.9±1.4	46.6±1.6	no
			MCS B	05 40 53.7	35 41 40	7.2±1.0	10.4±1.3	0.4
			S235 A	05 40 52.9	35 42 16	108±6.0	105±8.2	250
IRAS 06056+2131	152±4.5	232±6.6	MCS A	06 08 40.3	21 31 01	41.1±1.2	61.6±1.7	no
			MCS B	06 08 40.6	21 31 07	24.4±1.0	31.5±1.4	0.7
IRAS 06061+2151	55±2.5	134±4.2	MCS A	06 09 07.0	21 50 33	4.2±0.7	5.4±1.0	3.4
			MCS B	06 09 07.0	21 50 42	13.2±0.7	22.6±1.2	0.6
IRAS 06117+1350	86±2.9	60±2.4	MCS A	06 14 37.0	13 49 36	15.6±0.8	25.2±2.1	no(?)
			S269	06 14 37.9	13 49 38	50.7±2.4	< 8.7	640
IRAS 19442+2427	469±6.6	383±5.9	MCS A	19 46 19.4	24 35 24	7.0±0.9	9.7±1.0	no
			MCS B	19 46 20.6	24 35 39	19.8±1.0	30.5±1.1	no
			MCS C	19 46 21.3	24 35 47	16.7±1.4	18.0±1.6	no
			S87 all	19 46 20.1	24 35 29	374±7.3	256±7.7	570
			S87 core	39.3±1.0	40.4±1.1	29.7
IRAS 19446+2505	4200±30	3400±30	MCS A	19 46 46.6	25 13 01	145±9.8	151±20	no
			MCS B	19 46 47.5	25 13 14	219±17	157±27	no
			MCS C	19 46 48.4	25 12 20	867±29	934±55	no
			S88 B1	19 46 48.2	25 12 42	2180±22	1490±37	2500
			S88 B2	19 46 49.1	25 12 47	574±10	394±16	640

^a The total flux of the continuum emission larger than 3 σ level.

^b The position of peak flux of MCS identified from 110 GHz continuum image.

^c The total flux value of the associated CCSs at 8.4 GHz. “no” indicates no detection and “no(?)” indicates that high-angular observations has never been carried out.

TABLE 5
DERIVED PROPERTIES OF C¹⁸O CORES.

Region	T_{ex} (K)	core	$N(\text{H}_2)^a$ (10^{22} cm^{-2})	R_{core} (pc)	M_{core} (M_{\odot})	M_{vir} (M_{\odot})	$n(\text{H}_2)_{\text{core}}$ (10^5 cm^{-3})	Associated Objects		
								MCS ^b	NIR ^c	CCS ^d
IRAS 05375+3540	44	core A	2.3	0.035	2.6	6.2	2.1	...	1	...
		core B	3.6	0.027	2.9	5.2	5.2
		core C	3.2	0.034	3.7	9.9	3.2
		core D	3.1	0.020	1.8	3.0	7.8
		core E	1.1	0.026	0.9	1.7	1.7
		core F	0.9	0.019	0.5	1.1	2.3
		core G	1.8	0.022	1.2	1.6	3.8	...	1	...
		core H	3.7	0.027	3.2	6.9	5.7	B	1	1
		core I	5.1	0.042	6.2	16.8	2.9
		core J	8.9	0.026	6.5	9.4	12.8	A	1	...
		core K	2.6	0.022	1.8	2.7	5.8
		core L	2.0	0.015	1.2	1.8	12.1
		core M	2.0	0.045	4.6	5.3	1.8
		core N	3.1	0.047	6.5	7.4	2.2
		core O	1.0	0.010	0.5	... ^e	... ^e
		core P	5.0	0.035	6.1	6.4	5.0
		core Q	1.7	0.022	1.3	2.5	4.3
		core R	2.4	0.026	1.7	8.0	3.4
		core S	3.4	0.043	5.2	4.6	2.3	...	1	...
		core T	6.1	0.035	6.4	4.3	5.2	...	1	...
		core U	1.9	0.021	1.3	1.2	4.9
IRAS 06056+2131	35	core A	5.0	0.061	16.7	12.1	2.6
		core B	1.2	0.035	2.5	9.8	2.0
		core C	4.6	0.042	15.5	23.1	7.3
		core D	3.5	0.049	9.6	15.9	2.8
		core E	10.9	0.071	54.1	133.8	5.3	A	1	...
		core F	1.7	0.060	6.5	11.0	1.1	...	1	...
		core G	5.0	0.050	17.0	29.2	4.7
		core H	1.1	0.032	2.4	3.4	2.6
		core I	1.4	0.026	2.5	3.8	4.9
		core J	6.6	0.076	35.6	130.5	2.8	B	...	2
		core K	3.0	0.066	15.8	34.0	1.9	...	1	...
		core L	1.0	0.043	2.9	4.2	1.3
		core M	1.1	0.068	6.3	8.8	0.6	...	1	...
		core N	1.4	0.021	3.8	... ^e	... ^e
		core O	4.3	0.049	12.8	17.7	3.8
		core P	1.8	0.028	3.5	12.0	5.5
		core Q	1.8	0.035	3.8	3.8	3.1
		core R	2.6	0.032	5.0	5.1	5.4
		core S	3.4	0.064	14.4	17.5	1.9
IRAS 06061+2151	39	core A	2.1	0.036	4.2	9.3	3.1
		core B	1.9	0.036	4.4	6.4	3.3	...	1	...
		core C	0.9	0.040	2.3	1.8	1.2
		core D	1.5	0.043	3.9	11.4	1.7
		core E	1.8	0.045	5.4	6.8	2.1	...	1	...
		core F	1.6	0.050	4.8	7.9	1.3
		core G	1.4	0.037	3.4	6.3	2.3
		core H	2.4	0.021	5.0	... ^e	... ^e
		core I	1.8	0.057	6.7	7.3	1.3
		core J	1.2	0.051	4.0	3.6	1.0
		core K	1.1	0.039	2.9	2.9	1.7
		core L	2.0	0.026	3.9	4.0	7.7
		core M	1.5	0.036	4.1	11.4	3.0
		core N	1.2	0.027	2.8	2.1	4.9	...	1	...
		core O	7.5	0.043	19.4	94.4	8.5	B	2	2

TABLE 5—*Continued*

Region	T_{ex} (K)	core	$N(\text{H}_2)^a$ (10^{22} cm^{-2})	R_{core} (pc)	M_{core} (M_{\odot})	M_{vir} (M_{\odot})	$n(\text{H}_2)_{\text{core}}$ (10^5 cm^{-3})	Associated Objects		
								MCS ^b	NIR ^c	CCS ^d
IRAS 06117+1350	39	core P	2.6	0.040	5.4	62.3	3.0	A	1	1
		core Q	1.8	0.059	6.2	11.7	1.0
		core R	1.3	0.030	3.1	3.7	4.0	...	1	...
		core S	3.2	0.051	9.8	17.9	2.6
		core T	3.8	0.035	8.3	12.6	6.7
		core U	3.1	0.067	12.3	9.0	1.4
		core V	1.6	0.035	4.0	9.8	3.2
		core W	3.4	0.051	10.3	15.6	2.7
		core X	3.3	0.090	19.4	32.5	0.9
		core A	1.7	0.024	3.6	3.0	9.1
		core B	2.2	0.038	6.1	8.1	3.9
		core C	1.2	0.037	3.6	3.4	2.5
		core D	1.1	0.023	2.5	2.4	7.2
		core E	1.6	0.018	2.7	... ^e	... ^e
		core F	1.4	0.039	4.0	1.7	2.3
		core G	1.2	0.015	2.3	... ^e	... ^e
		core H	0.8	0.025	1.7	2.9	3.9
		core I	1.2	0.021	2.3	... ^e	... ^e
		core J	1.8	0.059	7.1	29.1	1.2
		core K	1.5	0.039	4.3	5.0	2.5
IRAS 19442+2427	44	core L	1.4	0.059	5.6	7.0	1.0
		core M	5.9	0.062	24.3	143.4	3.5	A	1	...
		core N	1.7	0.059	6.5	4.9	1.1
		core O	1.3	0.039	3.2	2.1	1.9
		core P	2.7	0.066	10.9	18.0	1.3
		core Q	1.6	0.054	6.4	10.7	1.4
		core R	1.7	0.043	4.6	3.0	2.0
		core S	0.8	0.014	1.6	... ^e	... ^e
		core T	0.9	0.024	3.2	1.4	8.0
		core U	0.9	0.030	2.1	1.8	2.7
		core V	2.1	0.068	10.1	20.3	1.1
		core W	1.4	0.015	2.7	... ^e	... ^e
		core X	1.6	0.042	4.2	25.6	2.0
		core Y	1.3	0.017	2.5	... ^e	... ^e
		core Z	1.3	0.044	3.8	1.7	1.5
		core AA	2.3	0.022	4.8	... ^e	... ^e
		core AB	2.0	0.020	3.8	... ^e	... ^e
		core A	2.2	0.027	2.4	3.2	4.2
		core B	1.2	0.031	1.1	1.7	1.3
		core C	2.5	0.028	2.8	3.5	4.5
		core D	6.1	0.039	9.1	14.1	5.3
		core E	3.3	0.047	6.2	6.6	2.1
		core F	6.4	0.051	12.4	6.9	3.3
		core G	2.2	0.025	2.1	2.4	4.7
		core H	2.5	0.026	1.8	3.1	3.6
		core I	5.7	0.038	4.9	7.3	3.1
		core J	5.7	0.050	9.8	12.9	2.7
		core K	5.3	0.056	10.4	10.7	2.1
		core L	1.5	0.012	0.8	... ^e	... ^e
		core M	2.7	0.032	3.6	7.7	3.8	...	1	...
		core N	8.8	0.051	15.7	25.7	4.1	A	(1) ^f	...
		core O	4.4	0.028	4.2	5.5	6.7
		core P	1.5	0.027	1.4	4.6	2.5
		core Q	3.6	0.036	5.3	6.6	3.9
		core R	5.2	0.049	10.4	15.5	3.1	A	(1) ^f	...

TABLE 5—*Continued*

Region	T_{ex} (K)	core	$N(\text{H}_2)^a$ (10^{22} cm^{-2})	R_{core} (pc)	M_{core} (M_{\odot})	M_{vir} (M_{\odot})	$n(\text{H}_2)_{\text{core}}$ (10^5 cm^{-3})	Associated Objects		
								MCS ^b	NIR ^c	CCS ^d
IRAS 19446+2505	60	core S	1.6	0.015	0.9	0.7	9.6
		core T	3.5	0.034	4.2	6.5	3.7
		core U	6.1	0.056	14.4	54.9	2.9	...	1	...
		core V	1.1	0.030	1.3	2.9	1.7
		core W	5.8	0.043	8.0	8.5	3.5	...	1	...
		core X	1.6	0.033	2.4	5.6	2.3
		core Y	1.5	0.013	0.9	... ^e	... ^e
		core Z	3.1	0.036	4.1	4.2	3.0
		core AA	7.5	0.048	9.7	30.4	3.1
		core AB	2.8	0.051	4.9	11.2	1.3
		core AC	18.2	0.047	14.1	37.2	4.7
		core AD	2.3	0.029	2.3	3.7	3.3
		core AE	2.4	0.025	2.2	3.1	5.0
		core AF	2.3	0.014	1.5	3.4	18.6
		core AG	5.2	0.046	7.6	14.1	2.7
		core AH	3.7	0.032	4.2	13.9	4.4	B
		core AI	1.0	0.020	1.1	1.9	4.8
		core AJ	1.1	0.019	0.7	1.7	3.8
		core AK	2.4	0.022	1.9	3.2	6.1	...	1	...
		core AL	5.0	0.039	5.8	3.3	3.4	...	1	...
		core A	2.0	0.010	1.0	... ^e	... ^e
		core B	2.2	0.025	1.9	4.4	4.3
		core C	2.0	0.018	1.7	2.0	10.0
		core D	5.2	0.036	8.8	24.1	6.0	...	1	...
		core E	10.6	0.042	15.0	17.2	7.1
		core F	2.5	0.010	1.4	... ^e	... ^e
		core G	1.7	0.019	1.3	2.2	6.5
		core H	1.6	0.022	1.5	2.6	4.8
		core I	1.6	0.017	1.1	1.9	7.9
		core J	1.9	0.023	1.4	2.4	3.9
		core K	3.8	0.026	3.4	5.0	6.7
		core L	5.4	0.040	7.7	13.3	4.2
		core M	1.8	0.024	1.7	3.4	4.3
		core N	2.0	0.015	1.3	2.6	13.2
		core O	2.4	0.027	1.9	3.2	3.3
		core P	2.5	0.026	2.4	5.9	4.8
		core Q	20.6	0.032	19.7	36.5	20.9
		core R	5.0	0.028	5.2	8.4	8.2
		core S	1.8	0.015	1.1	1.1	10.8
		core T	9.4	0.033	10.0	17.0	9.6
		core U	14.4	0.027	11.5	9.2	20.3
		core V	6.0	0.023	4.6	8.3	13.3
		core W	17.1	0.042	25.8	33.8	12.1
		core X	13.2	0.043	19.3	46.3	8.5
		core Y	5.4	0.038	6.7	9.2	4.2
		core Z	2.9	0.015	1.8	1.9	18.2
		core AA	2.1	0.010	1.2	... ^e	... ^e	...	1	...
		core AB	2.1	0.011	1.1	... ^e	... ^e
		core AC	2.8	0.023	2.2	6.3	6.1
		core AD	23.6	0.046	38.4	37.0	13.7
		core AE	3.4	0.019	2.3	4.6	11.6
		core AF	2.4	0.030	2.1	4.0	2.7
		core AG	3.9	0.021	2.7	8.0	10.0
		core AH	8.9	0.028	8.1	7.2	12.8
		core AI	4.9	0.013	3.0	... ^e	... ^e	...	1	...
		core AJ	8.8	0.045	15.1	19.8	5.8

TABLE 5—*Continued*

Region	T_{ex} (K)	core	$N(\text{H}_2)^a$ (10^{22} cm^{-2})	R_{core} (pc)	M_{core} (M_{\odot})	M_{vir} (M_{\odot})	$n(\text{H}_2)_{\text{core}}$ (10^5 cm^{-3})	Associated Objects		
								MCS ^b	NIR ^c	CCS ^a
		core AK	2.4	0.018	1.6	3.6	9.3
		core AL	2.2	0.017	1.5	3.6	10.7
		core AM	10.2	0.023	7.3	10.4	20.9
		core AN	5.1	0.020	3.7	12.2	16.3
		core AO	7.8	0.024	6.2	9.6	15.6

^aThe parameters at the intensity peak of cores.

^bThe name of the associated millimeter continuum source (MCS).

^cThe number of the associated 2MASS sources.

^dThe number of the associated centimeter continuum source.

^eValues cannot be derived since the radius has a large error.

^fThis source seems to be a foreground source (see text).

Table 6: Physical properties of MCSs.

Region	MCS	index ^a	Type ^b	R_d	T_d	M_d	n_{H_2}	Associated Objects	
				(pc)	(K)	(M_{\odot})	(10^5 cm^{-3})	NIR ^c	CCS ^d
IRAS 05375+3540	MCS A	3.3±0.3	D.T.	0.032	31.5	35.0	44.7	1	...
	MCS B	3.2±0.9	D.T.	0.019	31.5	9.3	46.1	1	1
IRAS 06056+2131	MCS A	3.5±0.2	D.T.	0.055	56.0	111	22.9	1	...
	MCS B	2.2±0.3	D.T.	0.037	54.0	64.1	42.6	...	2
IRAS 06061+2151	MCS A	2.2±1.2	D.T.	0.021	60.0	2.7	10.1	1	1
	MCS B	4.6±0.4	D.T.	0.033	60.0	35.6	35.8	2	2
IRAS 06117+1350	MCS A	4.2±0.4	D.T.	0.048	66.0	43.9	13.5	1	...
IRAS 19442+2427	MCS A	2.8±0.8	D.T.	0.021	43.5	9.1	34.1	(1) ^e	...
	MCS B	3.7±0.3	D.T.	0.018	77.0	14.1	80.6
	MCS C	0.6±0.4	F.F.	0.032	—	—	—
IRAS 19446+2505	MCS A	0.3±0.5	F.F.	0.050	—	—	—
	MCS B	−2.9±0.5 ^f	F.F.	0.057	—	—	—
	MCS C	0.6±0.2	F.F.	0.110	—	—	—

^a The spectral index is estimated from the flux densities at 98 GHz and 110 GHz.

^b The type of the continuum emission from MCSs. D.T. and F.F. denote dust thermal emission and free-free emission, respectively.

^c The number of the associated 2MASS sources.

^d The number of the associated centimeter continuum source.

^e This source seems to be a foreground source (see text).

^f The index would be underestimated (see text).

Table 7: Physical Properties of C¹⁸O clumps identified by Saito et al. (2007).

Region	clump	ΔV_{clump}	R_{clump} (pc)	M_{clump} (M_{\odot})	M_{vir} (M_{\odot})	$n(\text{H}_2)_{\text{clump}}$ ($\times 10^4 \text{ cm}^{-3}$)	core ^a
IRAS 05375+3540	clump B	1.5	0.16	80	79	6.8	A,B
	clump C	2.1	0.21	230	200	8.6	C-M,O
	clump D	1.6	0.21	170	120	6.4	N,P-U
IRAS 06056+2131	clump A	2.6	0.41	1000	560	5.0	A-S
IRAS 06061+2151	clump B	2.9	0.61	1300	1100	2.0	A-W
IRAS 06117+1350	clump C	2.3	0.37	380	390	2.6	D-F,K,L
	clump D	2.6	0.18	90	250	5.4	G-J,M,U
IRAS 19442+2427	clump A	2.6	0.29	380	400	5.6	A,C-O,R,T,U,AF,
	clump B	2.2	0.26	260	270	5.1	B,P,S,V,X,Y,AA-AD,AG,AI,AJ
	clump C	1.6	0.34	290	180	2.6	Q,W,Z,AE,AH,AK,AL
IRAS 19446+2505	clump B	2.6	0.22	460	320	15.0	A-AG,AI-AL,AN
	clump C	2.5	0.18	210	230	12.5	AH,AJ,AK,AO

^a The name of the associated C¹⁸O core.